Structural Investigation of Biomimetic Salicylate Complexes

Jitschaq A. van der Horn

January 19, 2018

Contents

1 Introduction

Iron complexes in non-heme enzymes are widely studied and described in literature. [1, 2, 3, 4, 5, 6, 7, 8, 9, 10, 11, 12, 13, 14, 15] A prominent example is salicylate 1,2-dioxygenase (SDO) which is involved in the biodegradation of aromatic molecules. [15, 4, 13] By QM/MM calculations Roy and Kästner explore the iron complex in the active site of this enzyme. [15] The Fe atom is coordinated by three histidine ligands, a bidentate salicylate ligand and an O_2 molecule in an octahedral geometry. The twice deprotonated salicylate is stabilized by hydrogen bonding between its carboxylate O-atoms and an arginine residue (Figure 1). [4]

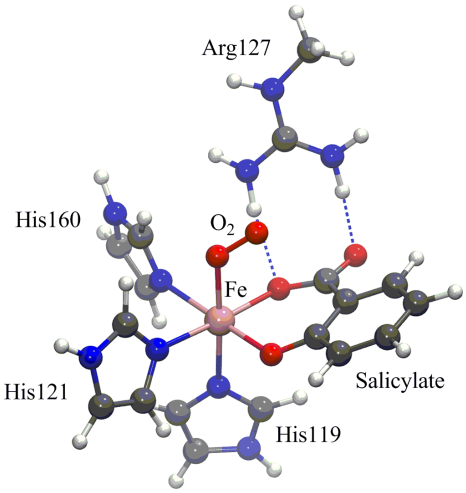

Figure 1: Model of the catalytic iron(II) centre of SDO including O_2 ligand, as calculated by Roy and Kästner. [15]

In the analysis of Roy and Kästner, the most energetically favourable ligand coordination was obtained. The crystal structure of naturally occuring SDO shows a slight difference regarding the coordination of the histidine residues (Figure 2). [4, 13]

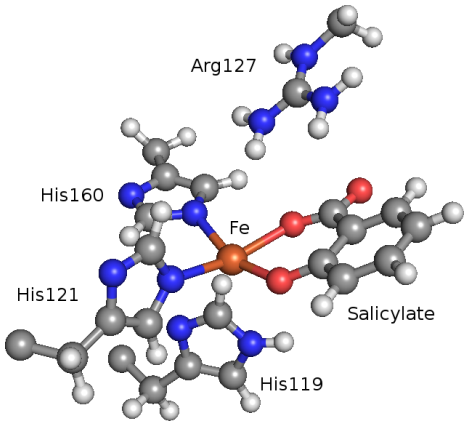

Figure 2: Crystal structure of the catalytic iron(II) centre of SDO without O_2 ligand, as found by Ferraroni et al. [4]

The complex facilitates the oxidation and ring cleavage of salicylate on the 1,2-position, as shown in Scheme 1. The catalytic activity of SDO is unique in the sense that it is able to cleave monohydroxylated compounds in the absence of an electron donating cofactor. Roy and Kästner found that the activation of salicylate and oxygen may be ascribed to strong covalent interactions between iron and both the salicylate compound and the oxygen molecule. This facilitates the partial shift of electron density from the salicylate to the oxygen, which results in an electronic structure "between the two limiting cases $Fe^{II} - O_2$ and $Fe^{II} - O_2^{\cdot -}$."[15] It remains yet unknown in what manner the salicylate compound is affected by this and how it is activated by its bidental coordination to iron.

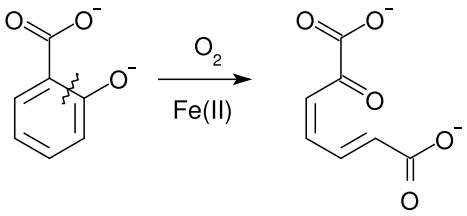

Scheme 1: Catalytic activity of SDO, showing cleavage of the phenyl ring on the 1,2-position [15]

In the study presented here, we attempt to get a better structural and chemical understanding of the catalytic site of SDO. The matter will be approached by synthesising and structurally characterising small-molecule metal-salicylate complexes. By using biomimetic metal complexes, one can gain *in vitro* insight in the catalytic activity of non-heme iron enzymes without the need for synthesizing and analyzing entire proteins. Such complexes provide low molecular weight analogues of the active site, which can help understand the structure-function relationship of enzymes and can also be used for developing new metal-based bioinspired catalysts. [1, 2, 3, 4, 5, 6, 7, 8] These complexes consist of a central metal ion which is coordinated by a number of ligands and by the substrate undergoing catalysis.

Free salicylic acid will first be crystallized and subjected to an X-ray crystal structure determination. Next, several complexes of salicylate with first-row transition metal atoms will be set out for synthesis, with the ultimate target being Fe(II) salicylate. If the obtained data are of sufficient resolution and quality, a topological analysis according to Bader's theory of Atoms in Molecules (AIM) [16] may be done in order to describe the metal binding effects in detail.

2 Salicylic acid

2.1 Introduction

To get a reference model for the salicylate complexes to be obtained, salicylic acid (Scheme 2) was crystallized and subjected to a charge-density study and a topological analysis. By using a multipole model for the electron density, one can derive a very detailed description of the molecular structure and reveal features such as bond strengths, provided that high-resolution data is used. We compare our crystal structure to a previously published paper by Munshi and Guru Row [17].

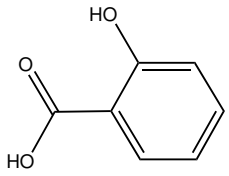

Scheme 2: Salicylic acid

2.2 Crystallization

Crystals of salicylic acid were prepared by making a saturated solution of salicylic acid in hot water, filtrating and slowly cooling down to room temperature. Salicylic acid crystallizes as extreme needles. The specimen for the current analysis was obtained by cutting of such a needle.

2.3 X-ray crystal structure determination

Data were obtained with a Bruker Kappa ApexII diffractometer (four circles with CCD detector) with sealed tube and Triumph monochromator, using Mo $K\alpha$ radiation. The temperature was controlled with an Oxford 700 Series Cryostream Cooler. Crystals were mounted using a MiTeGen 300 μm Dual-Thickness MicroLoop.

A total of 13284 images was collected with a detector distance of 40 mm and a rotation increment of $0.3°/frame$. Of theses, 5209 images were collected with an exposure time of 5 $s/frame$ and 8075 images with an exposure time of 30 $s/frame$.

Reflections were measured up to a resolution of $(\frac{\sin\theta}{\lambda})_{max} = 1.08$ Å^{-1}. Experimental details are given in Table 1. Intensities were integrated with the Eval15 software package. [18] Numerical absorption correction and scaling was done with Sadabs. [19] Equivalent reflections were defined by point group 2/m.

Table 1: Experimental details for salicylic acid

Molecular formula	$C_7H_6O_3$	
Formula weight	138.12	
Temperature	105(2) K	
Wavelength	0.71073 Å (MoKα)	
Crystal system, space group	Monoclinic, $P2_1/c$	
Unit cell dimensions	$a = 4.88330(19)$	$\alpha = 90°$
	$b = 11.2079(4)$	$\beta = 92.492(2)°$
	$c = 11.2582(5)$	$\gamma = 90°$
Volume	615.59(4) Å^3	
Z, Calculated density	4, 1.490 g/cm^3	
Absorption coefficient	0.12 mm^{-1}	
F(000)	288	
Crystal size	$150 \times 380 \times 80$ μm^3	
$(\frac{\sin\theta}{\lambda})_{max}$	1.08 Å^{-1}	
Limiting indices	-10 $\leq h \leq$ 10	
	-24 $\leq k \leq$ 24	
	-24 $\leq l \leq$ 23	
Refl. collected / unique / obs.	87033 / 6460 / 6083	[R_{int} = 0.0247]
Observed criteria	$I_{obs} > 0; I/\sigma_I > 0$	
Completeness to $\theta = 49.995°$	100%	
Number of parameters	271	
Number of restraints	0	
R1/wR2 [obs.]	0.0283 / 0.0223	
R1 [all refl.]	0.0389	
Goodness of Fit	1.7605	
Residual density [min/max]	-0.27 / 0.28 eÅ^{-3}	

The structure was solved with SHELXT. [20] Initial structure refinement was done with SHELXL on intensities with $I/\sigma_I > 2$. [21] Further refinement was done with the XD2016 program suite on reflections with $I/\sigma_I > 0$. [22] Refinement was done on F^2.

Refinement with XD was done in multiple steps. First, the overall scale factor was refined whilst leaving other parameters unmoved. All atom positions and anisotropic displacement parameters of the non-hydrogen atoms were then refined together with the positions and isotropic displacement parameters of the hydrogen atoms in the spherical atom model.

In the next refinement step, high resolution data ($(\frac{\sin\theta}{\lambda})_{min}$ = 0.81 Å^{-1}) were used to refine all non-hydrogen atom positions and anisotropic displacement parameters. Low-resolution data ($(\frac{\sin\theta}{\lambda})_{max}$ = 0.81 Å^{-1}) were subsequently used to refine only the hydrogen positions and istropic displacement parameters, based on generalized scattering factors which are polarized in the direction of the bond. [23, 24] Non-hydrogen positions and displacement parameters were then refined based on all reflections.

The structure was then refined with a multipole model for the electron density, as defined in equation 1. [25] The core and spherical valance scattering factors were obtained from Clementis Hartree-Fock Wavefunctions. [26] Multipole parameters — up to bond-oriented dipole for H; up to hexadecapole for C and O — were refined first with symmetry constraints and later freely for C and O.

In the final step, the κ and κ' parameter were refined for all C and O atoms, representing the multipole expansion and contraction. The same values for κ and κ' were used for all atoms of the same type.

In addition to our own data, the final XD refinement step of Munshi and Guru Row was repeated, using reflection data and model parameters from the supplemental data. [17]

$$\begin{aligned}\rho(\mathbf{r}) &= P_{core}\rho_{core}(r) + P_{val}\kappa^3\rho_{val}(\kappa r) \\ &+ \sum_{l=0}^{l_{max}} \kappa'^3 R_l(\kappa' r) \sum_{m=0}^{l} P_{lm\pm} Y_{lm\pm}(\Omega)\end{aligned} \tag{1}$$

Where ρ = electron density
r = distance from nucleus
P = population
κ = expansion coefficient
Y = spherical harmonical function

2.4 Data and model quality

The high resolution diffraction experiments of salicylic acid (Figure 3) has an overall completeness of 100% up to a maximum resolution of $(\frac{\sin\theta}{\lambda})_{max} = 1.08$ Å^{-1} and an average redundancy of 13. Refinement with SHELXL gave an R-value of 3.45%, which was improved with XD to 2.83%. It can be seen from the residual density plot (Figure 4) that still some residual density is left near the atom positions, similar to what was seen in the paper of Munshi and Guru Row (Figure 5). [17]

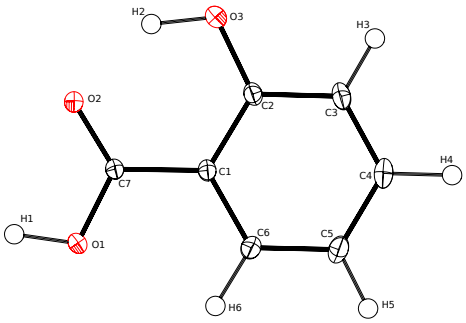

Figure 3: Displacement ellipsoid plot of H_2Sal, drawn at 50% probability level. Hydrogen atoms are drawn as solid spheres with arbitrary radius.

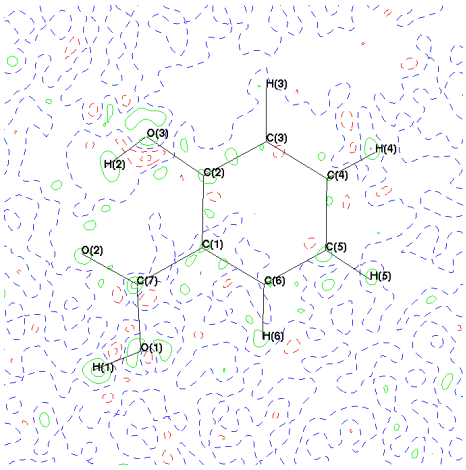

Figure 4: Residual electron density of H_2Sal after the refinement process with XD.
— Positive residual density
- - Negative residual density
- - Zero residual density
Contours are drawn at 0.10 eÅ^{-3}

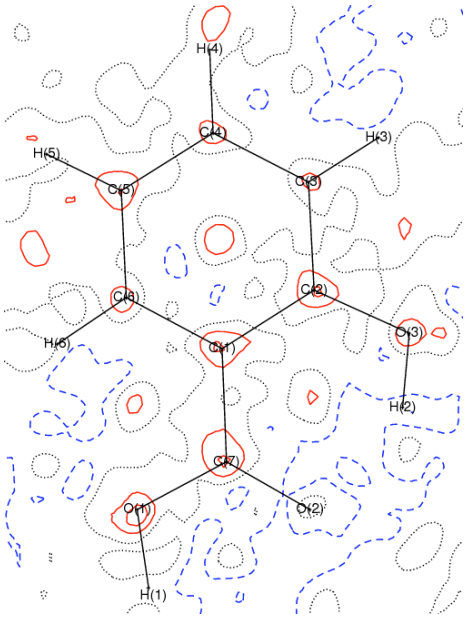

Figure 5: Residual electron density of H_2Sal after the refinement process with XD. The map was obtained from the publication of Munshi and Guru Row [17].
— Positive residual density
- - Negative residual density
· · · Zero residual density
Contours are drawn at 0.10 eÅ^{-3}

An ideal structural model should leave only noise in the residual electron density. Such noise is expected to follow a Gaussian distribution about zero. The gross residual number of electrons (eqn. 2) should be as close to zero as possible. [27] When the residual densities in both experiments are evaluated, we see in our data (Figure 6) a closer resemblance to a normal distribution as compared to the literature data (Figure 7). Furthermore, a lower gross residual number of electrons was observed in our experiment.

$$e_{gross} = \frac{V}{2N} \sum_{k=1}^{N} |\rho_0(k)| \tag{2}$$

Where V = physical volume of used grid
N = number of grid points
ρ_0 = residual density at grid point k

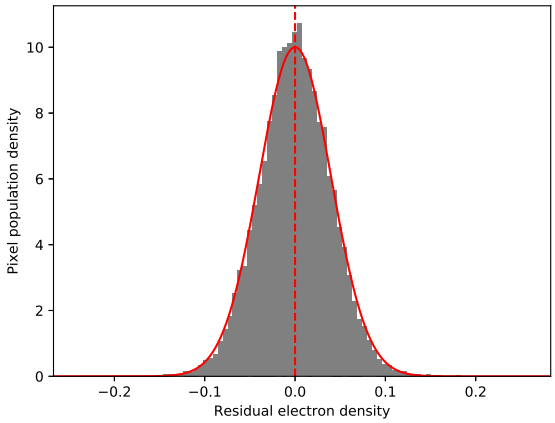

Figure 6: Analysis of the residual density in the unit cell using the program *Pixelanalysis* (Lutz, 2017). Residual electron density (eÅ^{-3}) is calculated with XDFFT [22] in a unit cell covering grid with a spacing of 0.2Å. Grid points are binned in ranges of 0.05 eÅ^{-3}. A gross residual number of 9.64 electrons (eqn. 2 [27]) was found in this plane.

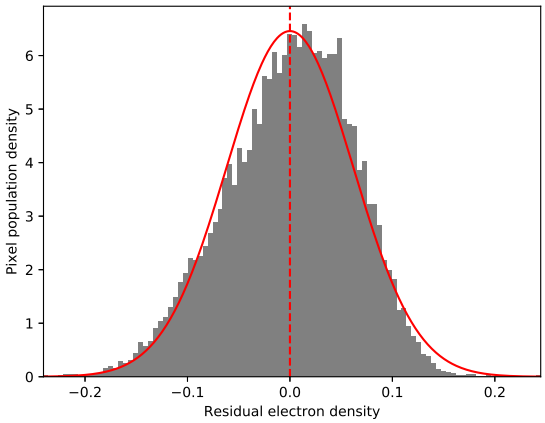

Figure 7: Analysis of the residual density in the unit cell using the program *Pixelanalysis* (Lutz, 2017). Residual electron density (eÅ^{-3}) is calculated with XDFFT [22] in a unit cell covering grid with a spacing of 0.2Å. The grid file was reconstructed from our own refinement based on available literature data. Grid points are binned in ranges of 0.05 eÅ^{-3}. A gross residual number of 15.29 electrons (eqn. 2 [27]) was found in this plane.

Analysis of the observed versus calculated reflection data from the original paper shows a non-linear relation between the two, where F_{obs} is weaker than F_{calc} for the strongest reflections. (Figure 8) This is a strong indication of extinction effects. The same analysis was performed on our own model and data, which showed a linear relation between the observed and calculated reflections. (Figure 9). This strongly indicates an improvement in data quality compared to the literature data [17].

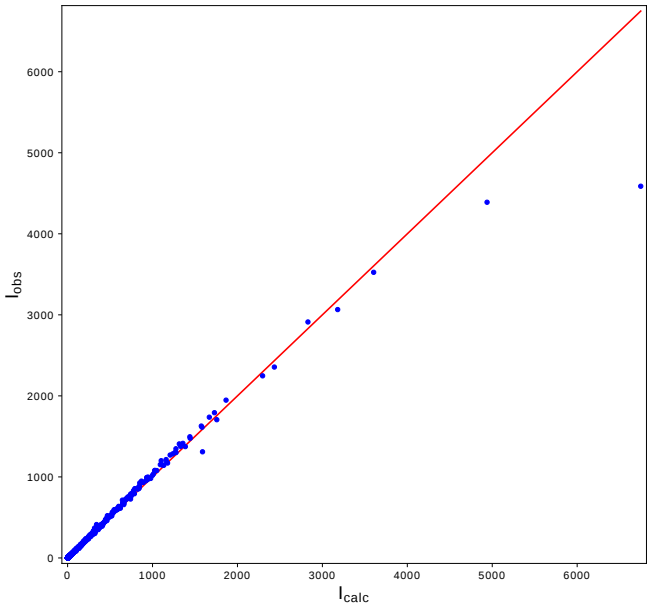

Figure 8: I_{obs} vs I_{calc} plot of the literature experiment. [17]

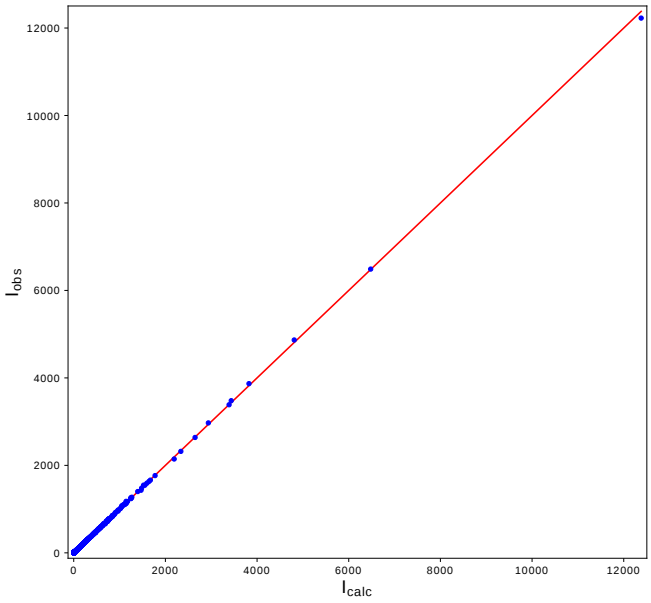

Figure 9: I_{obs} vs I_{calc} plot of the current experiment.

The physical relevance of the added multipole parameters can be clarified by a deformation density plot, as shown in Figure 10. The deformation density is the non-spherical contribution to the electron density, which can be visualized by subtracting the spherical model from the multipole model of the electron density. This graph shows features in the electron density model closely resembling bond electrons and lone pairs.

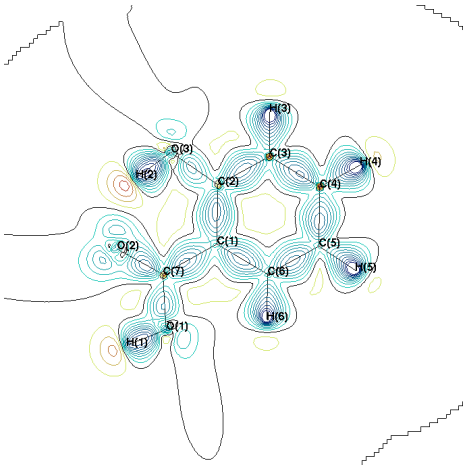

Figure 10: Static deformation density of the multipole model of H_2Sal after refinement with XD in the current study.
— Charge density excess
— Charge density deficit
— Zero-level
Contours are drawn at 0.10 eÅ^{-3}

2.5 Topological analysis

The electron density modeled by a multipole model can be used to analyze topological features in the crystal structure, following Bader's theory of Atoms in Molecules. [16] A trajectory plot was generated to visualize the electron density gradient in the molecule. (Figure 11) This plot shows critical (zero-flux) points in the electron density which can be found between all atoms and in ring-like atom combinations. The Laplacian ($\nabla^2\rho(r)$) of a bond critical point (BCP) in between two atoms can be used as an indication of the strength of this bond, where a larger absolute value represents a stronger bond.

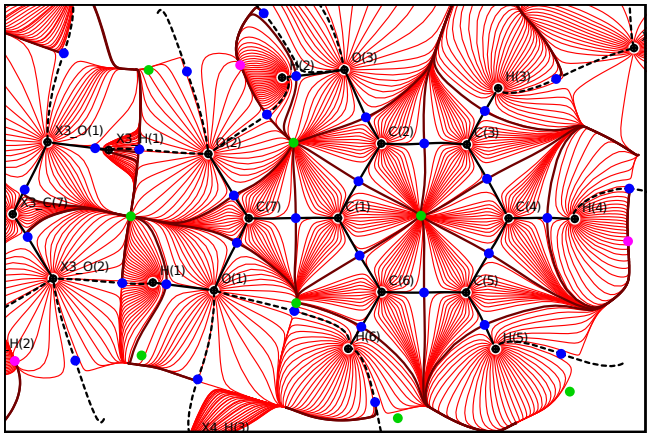

Figure 11: Trajectory plot of the first derivative of the electron density, dividing the molecule into atoms and showing the location of bond critical points in blue.

For all C-C and C-O bonds, the bond lengths and the Laplacian of the electron density at the bond critical points (BCP) were calculated. (Table 2) The calculations were performed with the XD module XDPROP. [22] Laplacian calculations with the XD module TOPXD yielded the same results. The values for the Laplacian of our model (3KAPHXDP) were compared to the values obtained by Munshi and Guru Row, both experimentally determined (LIT(EXP)) and obtained from DFT calculations (LIT(CALC)). [17]. It can be seen that our obtained values for the Laplacian seem to agree better with the theoretical values than the values experimentally obtained in the original paper, especially for the C(7)-O(1) single bond.

Table 2: Result of the bond critical point analysis of H_2Sal. Columns labeled Lit were determined by Munshi and Guru Row. [17]

i	j	d_i (Å)	d_j (Å)	d_{i+j} (Å)	$i-j$ (Å)	3KAPHXDP $\nabla^2\rho$	LIT(EXP) $\nabla^2\rho$	LIT(CALC) $\nabla^2\rho$
C(2)	- O(3)	0.4993	0.8554	1.3547	1.3529(2)	-21.00(6)	16.50(4)	16.54
C(7)	- O(1)	0.4486	0.8644	1.3130	1.3128(2)	-19.18(8)	32.43(7)	21.49
C(7)	- O(2)	0.4445	0.8009	1.2454	1.2452(2)	-30.05(9)	31.03(9)	30.38
C(7)	- C(1)	0.7708	0.6943	1.4650	1.4650(2)	-16.17(2)	16.12(3)	14.51
C(1)	- C(2)	0.6896	0.7219	1.4115	1.4112(2)	-18.62(2)	-19.75(3)	-18.23
C(2)	- C(3)	0.7032	0.6974	1.4007	1.4004(3)	-19.84(2)	-19.24(3)	-19.18
C(3)	- C(4)	0.6539	0.7356	1.3895	1.3893(3)	-20.19(3)	-17.73(3)	-17.42
C(4)	- C(5)	0.6611	0.7412	1.4022	1.4022(3)	-18.87(3)	-18.61(3)	-17.56
C(5)	- C(6)	0.6890	0.6956	1.3846	1.3846(3)	-19.44(2)	-18.98(3)	-19.40
C(6)	- C(1)	0.6971	0.7087	1.4057	1.4056(3)	-19.01(2)	-16.41(3)	-15.24

To put this in perspective, several other refinement models were used for a Laplacian calculation. In the original paper, the authors use a different multipole model in which the κ and κ' values for O(2) and C(7) are refined independently and with the maximum multipole set at the octapole level. This procedure was repeated with literature data (REPRO). [17]. For comparison, our final model (3KAPHXDP) was modified several times to include the same additional κ and κ' parameters (5KAP____) as well as both multipole (octapole and hexadecapole) levels (____OCTP and ____HXDP). In additional models the hydrogen atoms were fixed to distances observed in neutron-scattering with their isotropic displacement parameters (IDP) to be 1.2 times the IDP of the neighbouring carbons and 1.5 times the IDP of the neighbouring oxygens, respectively (HFIX____). Finally, the displacement parameters of hydrogen were anisotropically calculated by the SHADE server [28] (SHAD____). The result of the analysis is visualized in Figure 12.

Although the values of the Laplacian do seem to agree in general, they highly depend on the used model. This makes it difficult to draw any solid conclusions from this analysis. The discrepancies are most evident in the very polar C-O bonds, especially in the carboxylate group. Intuitively one would expect the C(7)=O(2) double bond to be stronger than the other bonds, which can indeed be seen in the DFT calculations. This is in agreement with our final model (3KAPHXDP).

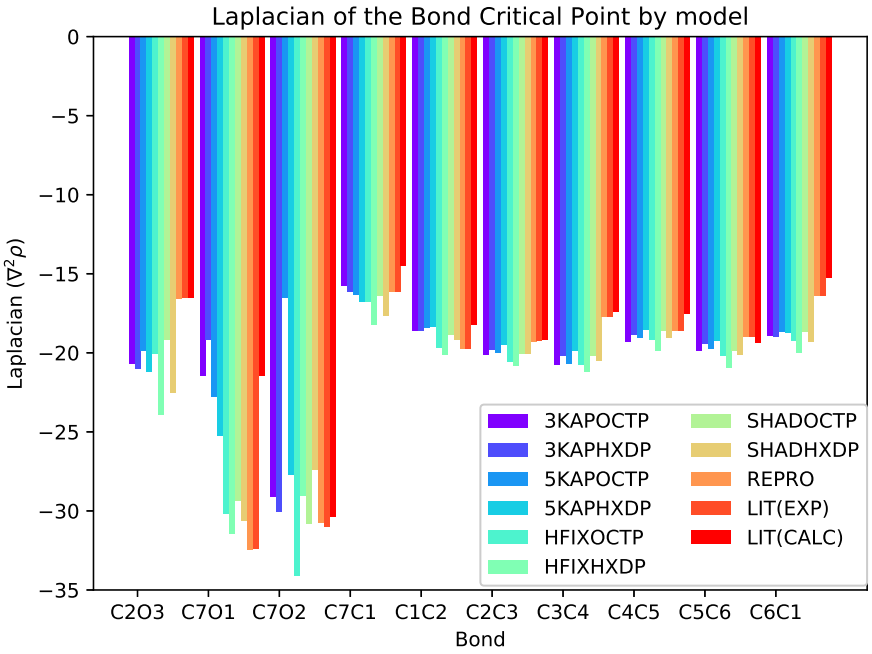

Figure 12: Comparison of the Laplacian at the Bond Critical Points obtained from the topological analysis of various electron density models (including Table 2). See text for a clarification of the labels.

From the aromatic C-C bond lengths, we can learn something about the stability of the aromatic ring. It is known from literature that single substituents on benzene molecules increase the length of the adjacent C-C bonds. [29] A statistical analysis of the aromatic bonds in salicylic acid shows that the C(1)-C(2) bond is significantly longer and thus less stable than the other bonds. (Table 3) This could explain why this bond is broken during the oxidation reaction in SDO. We did not convincingly see this phenomenon in the bond strengths from the Laplacian analysis.

Table 3: Bond length comparison of the C(1)-C(2) bond to the other aromatic bonds. Differences in bond length (Λ) are defined as $\frac{\Delta}{\sigma}$ where $\Delta(\text{Å}) = |i-j| - |C(1)-C(2)|$ and $\sigma(\text{Å}) = \sqrt{\sigma_i^2 + \sigma_j^2}$.

i	j	$i-j$ (Å)	Δ	σ	Λ
C(1)	- C(2)	1.4112(2)			
C(2)	- C(3)	1.4004(3)	-0.0108	0.00036	-29.95
C(3)	- C(4)	1.3893(3)	-0.0219	0.00036	-60.74
C(4)	- C(5)	1.4022(3)	-0.0090	0.00036	-24.96
C(5)	- C(6)	1.3846(3)	-0.0266	0.00036	-73.78
C(6)	- C(1)	1.4056(3)	-0.0056	0.00036	-11.53

2.6 Conclusions

Salicylic acid was successfully crystallized and its structure was solved and refined from a high-resolution X-ray diffraction data set. Comparison with literature data [17] shows a significant improvement in data and model quality. This follows mainly from the I_{obs} vs. I_{calc} relation and the residual electron density distribution, which have both improved in our experiment.

A topological analysis indicates bond length variations in the aromatic ring and provides a clue for the salicylate oxidation reaction in SDO. The bond at which oxidation takes place in salicylate is the longest of all aromatic bonds (C(1)-C(2)), making this specific bond a relevant point of focus in following experiments.

Bond strengths, which are measured as the Laplacian ($\nabla^2\rho(r)$) at the bond critical points, are dependent on the used multipole model. The Laplacian values obtained from our final model are in good correspondence with the values based on DFT-calculations from literature [17]. Topological analyses of metal-coordinated salicylate complexes in chapter 3 will show if this value can be used for a bond strength comparison. The final model serves as a solid base for comparison with metal-salicylate complexes.

3 Metal coordination effects

3.1 Introduction

To better understand the effects of metal coordination on salicylic acid, crystals of metal salicylate complexes were set out for synthesis. By subjecting the crystal structures of these complexes to a toplogical analysis in the same manner as salicylic acid, the effect of metal-coordination can hopefully be determined. Based on the findings in the previous chapter, we expect to see a change in the C(1)-C(2) bond distances. Several crystal structures of metal(II)-salicylate complexes without counterions are known from the literature. [30, 31] No such structures are known with iron as the metal. During the course of this study, two diffraction data sets of these metal-salicylate complexes were obtained with sufficient data quality for a topological analysis. In this chapter, we will discuss the crystal structures of *manganese(II) salicylate dihydrate* (Scheme 3) and *zinc(II) salicylate dihydrate* (Scheme 4). A comparison will made between the aromatic bonds in each of the salicylate ligands and the equivalent bonds in free salicylic acid.

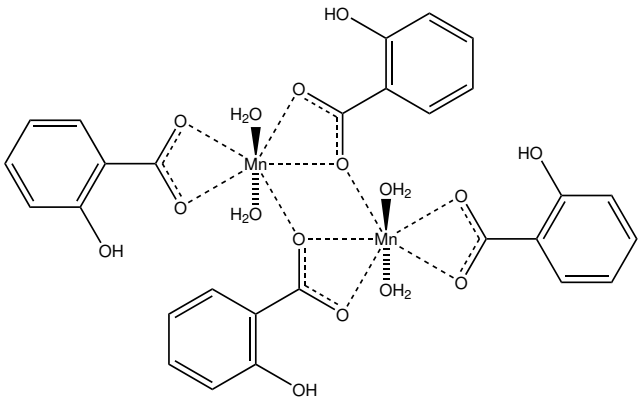

Scheme 3: Manganese(II) salicylate dihydrate

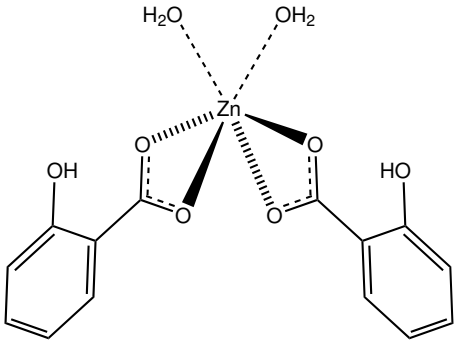

Scheme 4: Zinc(II) salicylate dihydrate

3.2 Manganese(II) salicylate dihydrate

3.2.1 Synthesis and crystallization

The synthesis procedure was adapted from Rissanen et al. [30] 1.69 g $Mn(SO_4)_2 \cdot H_2O$ was dissolved in 100 mL H_2O while stirring. 1.60 g Sodium salicylate was added to the solution until completely dissolved. The solution was brought into a capped Petri dish and left to crystallize. After seven days, crystals suitable for X-ray diffraction had formed.

3.2.2 X-ray crystal structure determination

A total of 9286 images was collected with a detector distance of 40 mm and a rotation increment of $0.5°/frame$. Of these, 4362 images were collected with an exposure time of 10 $s/frame$ and 4924 images with an exposure time of 40 $s/frame$. The X-ray generator was set to 50 kV and 30 mA.

Reflections were measured up to a resolution of $(\frac{\sin\theta}{\lambda})_{max} = 1.08$ Å^{-1}. Experimental details are given in Table 4. Intensities were integrated with the Eval15 software package. [18] A mosaicity of 0.4 was used for the integration. Numerical absorption correction and scaling was done with Sadabs. [19] Equivalent reflections were defined by point group 2/m.

The structure was solved with SHELXT. [20] Initial structure refinement was done with SHELXL on intensities with $I/\sigma_I > 2$. [21] Further refinement was done with the XD2016 program suite on reflections with $I/\sigma_I > 0$ in the same manner as the structure refinement of salicylic adid. [22] Refinement was done on F^2.

Table 4: Experimental details for manganese(II) salicylate dihydrate

Molecular formula	$Mn(C_7H_5O_3)_2(H_2O)_2$	
Formula weight	730.38	
Temperature	100(2) K	
Wavelength	0.71073 Å (MoKα)	
Crystal system, space group	Monoclinic, $P2_1/c$	
Unit cell dimensions	$a = 15.4901(8)$	$\alpha = 90°$
	$b = 12.2829(6)$	$\beta = 96.698(2)°$
	$c = 7.5509(3)$	$\gamma = 90°$
Volume	1426.85(12) Å^3	
Z, Calculated density	2, 1.700 g/cm^3	
Absorption coefficient	0.97 mm^{-1}	
F(000)	748	
Crystal size	$40 \times 135 \times 200$ μm^3	
$(\frac{\sin\theta}{\lambda})_{max}$	1.08 Å^{-1}	
Limiting indices	-33 $\leq h \leq$ 33	
	-26 $\leq k \leq$ 26	
	-16 $\leq l \leq$ 16	
Reflections collected / unique / obs.	255527 / 14971 / 11696	[R_{int} = 0.0385]
Observed criteria	$I_{obs} > 0; I/\sigma_I > 0$	
Completeness to $\theta = 50.009°$	100%	
Number of parameters	791	
Number of restraints	0	
R1/wR2 [obs.]	0.0165 / 0.0202	
R1 [all refl.]	0.0359	
Goodness of Fit	1.4797	
Residual density [min/max]	-0.24 / 0.70 eÅ^{-3}	

3.2.3 Crystal structure

Manganese(II) salicylate dihydrate crystallizes in space group $P2_1/c$. [30] The complex is dimeric and consists of two assymetric units which are related via inversion symmetry. The asymmetric unit contains a single manganese centre which is coordinated by two water molecules and two salicylate ligands via their carboxylate groups. The manganese atom is additionally coordinated to a symmetry related salicylate ligand, making a total of seven coordinated oxygen atoms. (Figure 13) Each salicylate ligand is deprotonated at the carboxylate group, which is in agreement with the oxidation state of +2 for manganese.

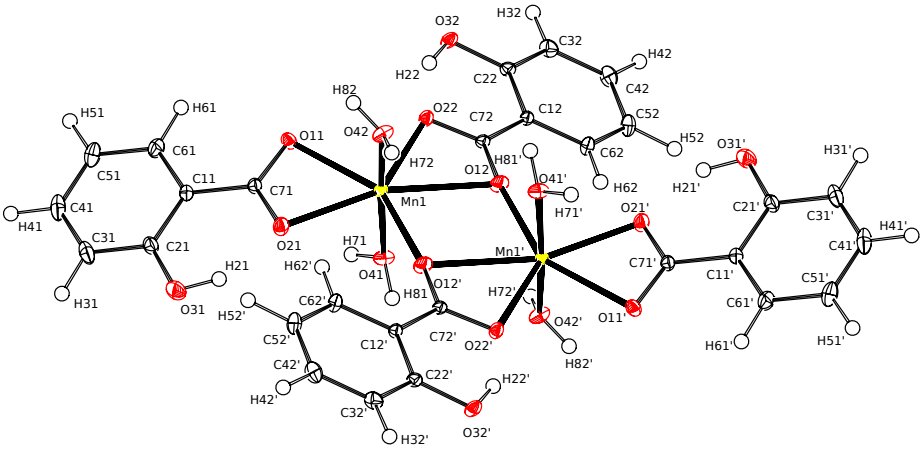

Figure 13: Displacement ellipsoid plot of $Mn(HSal)_2(H_2O)_2$, drawn at 50% probability level. Hydrogen atoms are drawn as solid spheres with arbitrary radius. Symmetry code: $i : 1-x, 1-y, 1-z$

3.2.4 Data and model quality

The high resolution diffraction experiments of manganese salicylate, has an overall completeness of 100% up to a maximum resolution of $(\frac{\sin\theta}{\lambda})_{max} = 1.08$ Å^{-1} and an average redundancy of 17. Initial refinement with SHELXL resulted in an R-value of 2.46%. Further refinement with XD lead up to a final R-value of 1.65%. It can be seen from the residual density plot (Figure 14) that most features have been included in the electron density model. Together with the relatively small displacement ellipsoids (Figure 13), this is a strong indication of high data quality.

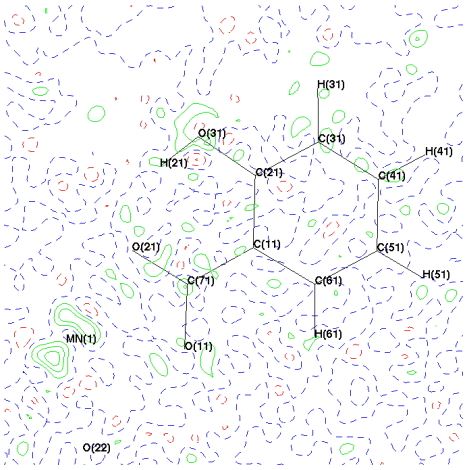

Figure 14: Residual electron density of $Mn(HSal)_2(H_2O)_2$ after the refinement process with XD. Fourier ripples can be seen around the Mn atom.
— Positive residual density
- - Negative residual density
- - Zero residual density
Contours are drawn at 0.10 eÅ^{-3}

3.2.5 Topological analysis

We analyzed the lengths and strengths of all intramolecular bonds with XDPROP. [22] (Table 5) In both salicylate ligands, the longest aromatic bonds are the C(1_)-C(2_) bonds, which agrees with what we expect based on our observations in free salicylic acid. The bond strength, expressed as the Laplacian at the Bond Critical Point, indicates that these bonds are indeed the weakest of all aromatic bonds.

Table 5: Result of the bond critical point analysis of $Mn(HSal)_2(H_2O)_2$.

i	j	d_i (Å)	d_j (Å)	d_ij (Å)	$i-j$ (Å)	$\nabla^2\rho$ BCP
C(21)	- O(31)	0.4751	0.8773	1.3524	1.3514(5)	-19.30(10)
C(71)	- O(11)	0.4456	0.8346	1.2802	1.2800(4)	-22.24(9)
C(71)	- O(21)	0.4491	0.8232	1.2723	1.2722(4)	-26.72(9)
C(71)	- C(11)	0.7390	0.7357	1.4748	1.4747(4)	-15.11(3)
C(11)	- C(21)	0.7015	0.7099	1.4114	1.4113(5)	-17.06(3)
C(21)	- C(31)	0.7298	0.6713	1.4012	1.4008(5)	-20.39(3)
C(31)	- C(41)	0.6414	0.7458	1.3871	1.3863(7)	-20.39(4)
C(41)	- C(51)	0.7278	0.6719	1.3998	1.3994(7)	-20.08(4)
C(51)	- C(61)	0.7092	0.6758	1.3850	1.3844(5)	-20.17(3)
C(61)	- C(11)	0.7072	0.6959	1.4031	1.4031(5)	-18.12(3)
Mn(1)	- O(11)	1.1622	1.1821	2.3443	2.3439(3)	+3.681(2)
Mn(1)	- O(21)	1.1088	1.1449	2.2537	2.2535(3)	+4.748(3)
C(22)	- O(32)	0.4941	0.8753	1.3694	1.3692(4)	-16.45(8)
C(72)	- O(12)	0.4297	0.8294	1.2591	1.2591(4)	-14.77(9)
C(72)	- O(22)	0.4427	0.8352	1.2779	1.2775(4)	-18.90(9)
C(72)	- C(12)	0.7492	0.7322	1.4813	1.4812(4)	-14.97(3)
C(12)	- C(22)	0.6839	0.7232	1.4071	1.4066(4)	-17.93(3)
C(22)	- C(32)	0.7197	0.6754	1.3951	1.3950(4)	-19.94(3)
C(32)	- C(42)	0.7187	0.6718	1.3905	1.3902(5)	-20.13(3)
C(42)	- C(52)	0.7110	0.6885	1.3994	1.3993(5)	-18.27(3)
C(52)	- C(62)	0.6831	0.7063	1.3894	1.3890(5)	-20.44(3)
C(62)	- C(12)	0.7001	0.7019	1.4020	1.4018(4)	-18.18(3)
Mn(1)	- O(12)	1.2779	1.2654	2.5433	2.5400(3)	+2.139(2)
Mn(1)	- O(22)	1.1227	1.0917	2.2143	2.2143(3)	+5.158(2)

A statistical analysis was done for each of the salicylate ligands to compare the length of the C(1_)-C(2_) bond to the other aromatic bonds. (Table 6) This analysis shows that this bond is indeed significantly longer than the other aromatic bonds.

Table 6: Bond length comparison of the C(1_)-C(2_) bond to the other aromatic bonds in each salicylate ligand. Differences in bond length (Λ) are defined as $\frac{\Delta}{\sigma}$ where $\Delta(\text{Å}) = |i-j| - |(1\_) - C(2\_)|$ and $\sigma(\text{Å}) = \sqrt{\sigma_i^2 + \sigma_j^2}$.

i	j	$i-j$ (Å)	Δ	σ	Λ
C(11)	- C(21)	1.4113(5)			
C(21)	- C(31)	1.4008(5)	-0.0105	0.00071	-14.85
C(31)	- C(41)	1.3863(7)	-0.0250	0.00086	-29.06
C(41)	- C(51)	1.3994(7)	-0.0119	0.00086	-13.83
C(51)	- C(61)	1.3844(5)	-0.0269	0.00071	-38.04
C(61)	- C(11)	1.4031(5)	-0.0082	0.00071	-11.60
C(12)	- C(22)	1.4066(4)			
C(22)	- C(32)	1.3950(4)	-0.0116	0.00057	-20.51
C(32)	- C(42)	1.3902(5)	-0.0164	0.00064	-25.61
C(42)	- C(52)	1.3993(5)	-0.0073	0.00064	-11.40
C(52)	- C(62)	1.3890(5)	-0.0176	0.00064	-27.49
C(62)	- C(12)	1.4018(4)	-0.0048	0.00057	-8.49

3.3 Zinc(II) salicylate dihydrate

3.3.1 Synthesis and crystallization

Zinc(II) salicylate dihydrate was prepared via the gel crystallization technique. [32]

14.8 g Zinc nitrate hexahydrate (50 mmol) was dissolved in 45 mL water. 5 mL Tetramethoxysilane is added and the suspension is heavily stirred until it becomes clear. The solution is filled into plastic tubes and stored overnight.

The supernatant solution was prepared by suspending 6.7 g salicylic acid in 50 mL water. The pH was then adjusted with concentrated NaOH (19 M) to pH = 5.4. Nearly all of the acid was dissolved and the solution was filtrated.

3.3.2 X-ray crystal structure determination and refinement

A total of 14611 images was collected with a detector distance of 45 mm and a rotation increment of $0.5°/frame$. Of these, 11414 images were collected with an exposure time of 10 $s/frame$ and 3197 images with an exposure time of 45 $s/frame$.

Reflections were measured up to a resolution of $(\frac{\sin\theta}{\lambda})_{max} = 1.07$ Å^{-1}. Experimental details are given in Table 7. Intensities were integrated with the Eval15 software package. [18] Numerical absorption correction and scaling was done with Sadabs. [19] Equivalent reflections were defined by point group 2/m.

The structure was solved with SHELXT. [20] Initial structure refinement was done with SHELXL on intensities with $I/\sigma_I > 2$. [21] The zinc-atom was fixed on the coordinates $xyz = (0, 0.6802, 0.5)$. Further refinement was done with the XD2016 program suite on reflections with $I/\sigma_I > 0$ in the same manner as the structure refinement of salicylic adid. [22] Refinement was done on F^2.

Table 7: Experimental details for zinc(II) salicylate dihydrate

Molecular formula	$Zn(C_7H_5O_3)_2(H_2O)_2$	
Formula weight	738.88	
Temperature	100(2) K	
Wavelength	0.71073 Å (MoKα)	
Crystal system, space group	Monoclinic, $C2$	
Unit cell dimensions	$a = 15.4510(7)$	$\alpha = 90°$
	$b = 5.3650(2)$	$\beta = 93.1490(10)°$
	$c = 8.9270(5)$	$\gamma = 90°$
Volume	738.88(6) Å^3	
Z, Calculated density	2, 1.688 g/cm^3	
Absorption coefficient	1.70 mm^{-1}	
F(000)	384	
Crystal size	$40 \times 150 \times 170$ μm^3	
$(\frac{\sin\theta}{\lambda})_{max}$	1.07 Å^{-1}	
Limiting indices	$-32 \leq h \leq 32$	
	$-11 \leq k \leq 11$	
	$-19 \leq l \leq 19$	
Reflections collected / unique / obs.	81167 / 7480 / 7466	[$R_{int} = 0.0196$]
Completeness to $\theta = 49.202°$	100%	
Observed criteria	$I_{obs} > 0; I/\sigma_I > 0$	
Number of parameters	398	
Number of restraints	0	
R1/wR2 [obs.]	0.0114 / 0.0132	
R1 [all refl.]	0.0116	
Goodness of Fit	1.3955	
Residual density [min/max]	-0.36 / 1.14 eÅ^{-3}	

3.3.3 Crystal structure

Zinc(II) salicylate dihydrate is known from the literature to crystallize in space group $C2$. [30] The complex consists of a single zinc atom which is sixfold coordinated to two water molecules and two salicylate ligands via the carboxylate group. The salicylate ligands are both deprotonated at the carboxylate group, which corresponds to the oxidation state of +2 for zinc. The ligands are symmetry related via a C_2 rotation axis which passes through the zinc atom. (Figure 15)

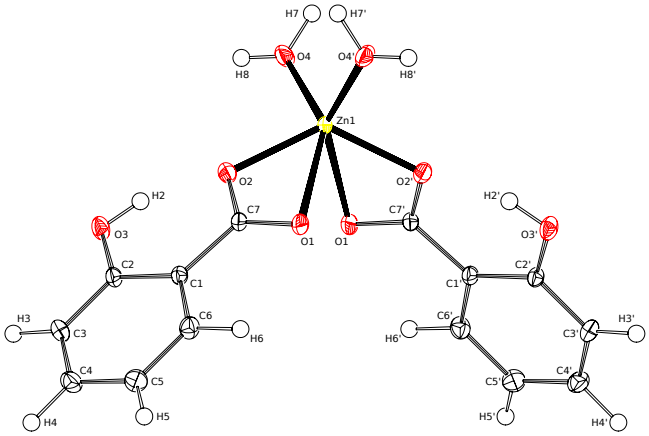

Figure 15: Displacement ellipsoid plot of $Zn(HSal)_2(H_2O)_2$, drawn at 50% probability level. Hydrogen atoms are drawn as solid spheres with arbitrary radius. Symmetry code: $i : -x, y, 1 - z$

3.3.4 Data and model quality

The high resolution diffraction experiments of zinc salicylate has an overall completeness of 100% up to a maximum resolution of $(\frac{\sin\theta}{\lambda})_{max} = 1.07$ Å^{-1} and an average redundancy of 10. The SHELXL refinement reached an R-value of 1.52%, which decreased to 1.14% after refinement with XD. It can be seen from the residual density plot (Figure 16) that most features have been included in the electron density model. Together with the relatively small displacement ellipsoids (Figure 15), this is a strong indication of high data quality.

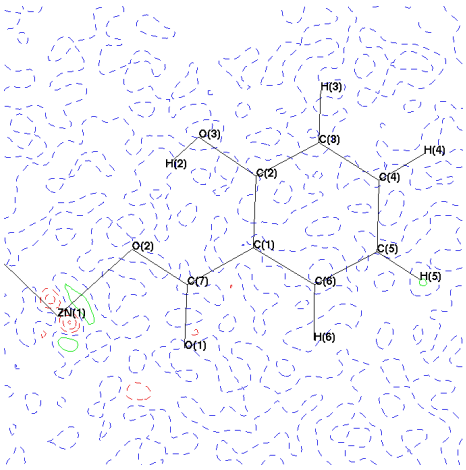

Figure 16: Residual electron density of $Zn(HSal)_2(H_2O)_2$ after the refinement process with XD.
— Positive residual density
- - Negative residual density
- - Zero residual density
Contours are drawn at 0.10 eÅ^{-3}

3.3.5 Topological analysis

The bond lengths and bond strengths were calculated with XDPROP. [22] (Table 8) Interestingly, no critical point was found between Zn(1) and O(1), which is also apparent from the gradient trajectory plot (Figure 17). This may explain the long distance between these atoms, which is not to be expected for bonded atoms.

Table 8: Result of the bond critical point analysis of $Zn(HSal)_2(H_2O)_2$.

i	j	d_i (Å)	d_j (Å)	d_ij (Å)	$i-j$ (Å)	$\nabla^2\rho$ BCP
C(2)	- O(3)	0.5107	0.8512	1.3619	1.3616(4)	-20.95(10)
C(7)	- O(1)	0.4612	0.7902	1.2514	1.2512(4)	-34.92(14)
C(7)	- O(2)	0.4783	0.8111	1.2895	1.2893(4)	-27.86(12)
C(7)	- C(1)	0.7504	0.7340	1.4844	1.4841(4)	-16.77(4)
C(1)	- C(2)	0.6847	0.7218	1.4065	1.4063(3)	-19.12(3)
C(2)	- C(3)	0.7421	0.6568	1.3989	1.3985(4)	-20.85(5)
C(3)	- C(4)	0.7081	0.6818	1.3899	1.3897(4)	-18.67(4)
C(4)	- C(5)	0.7119	0.6899	1.4018	1.4017(5)	-20.14(4)
C(5)	- C(6)	0.6851	0.7026	1.3877	1.3876(4)	-19.48(4)
C(6)	- C(1)	0.7065	0.6970	1.4035	1.4026(4)	-22.05(5)
Zn(1)	O(1)				2.5685(3)	
Zn(1)	- O(2)	0.9807	1.0107	1.9914	1.9905(3)	+8.875(4)

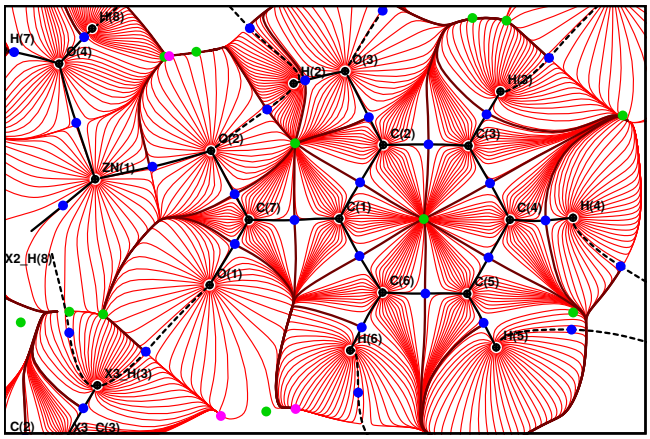

Figure 17: Trajectory plot of the first derivative of the electron density, dividing the molecule into atoms and showing the location of bond critical points in blue.

In the salicylate ligand, the C(1)-C(2) bond is the longest of the aromatic bonds, but this is not represented by the Laplacian in this case. A statistical analysis shows the difference in bond distances between C(1)-C(2) and the other aromatic rings in terms of the standard deviation. (Table 9) From this analysis, it can be concluded that the C(1)-C(2) bond is significantly longer than the other aromatic bonds, which agrees with our previous findings.

Table 9: Bond length comparison of the C(1)-C(2) bond to the other aromatic bonds. Differences in bond length (Λ) are defined as $\frac{\Delta}{\sigma}$ where $\Delta(\text{Å}) = |i-j| - |C(1)-C(2)|$ and $\sigma(\text{Å}) = \sqrt{\sigma_i^2 + \sigma_j^2}$.

i	j	$i-j$ (Å)	Δ	σ	Λ
C(1)	- C(2)	1.4063(3)			
C(2)	- C(3)	1.3985(4)	-0.0078	0.00050	-15.60
C(3)	- C(4)	1.3897(4)	-0.0166	0.00050	-33.20
C(4)	- C(5)	1.4017(5)	-0.0046	0.00058	-7.89
C(5)	- C(6)	1.3876(4)	-0.0187	0.00050	-37.40
C(6)	- C(1)	1.4026(4)	-0.0037	0.00050	-7.40

3.4 Comparison

With a topological analysis performed on salicylic acid and two related metal complexes, it may be interesting to see if there is any notable effect of the metal coordination on the aromatic bond lengths. An analysis of the aromatic bond lengths (Table 10) in both complexes shows the changes in bond length (Table 11) as compared to free salicylic acid. The most significant change is in the C(1)-C(2) bond of the Zn-coordinated salicylate. However, this bond length (1.4063(3)Å) is nearly identical to the equivalent bond in the second Mn-coordinated salicylate ligand (1.4066(4)Å). Therefore, based on the available data, it cannot be conclusively stated that the coordination to Mn or Zn has a significant impact on the bond lengths in salicylic acid.

Table 10: Overview of the aromatic bond lengths (Å) in salicylic acid and the metal-coordinated salicylate ligands

	C(1)-C(2)	C(2)-C(3)	C(3)-C(4)	C(4)-C(5)	C(5)-C(6)	C(6)-C(1)
H_2Sal	1.4112(2)	1.4004(3)	1.3893(3)	1.4022(3)	1.3846(3)	1.4056(3)
MnSal (_1)	1.4113(5)	1.4008(5)	1.3863(7)	1.3994(7)	1.3844(5)	1.4031(5)
MnSal (_2)	1.4066(4)	1.3950(4)	1.3902(5)	1.3993(5)	1.3890(5)	1.4018(4)
ZnSal	1.4063(3)	1.3985(4)	1.3897(4)	1.4017(5)	1.3876(4)	1.4026(4)

Table 11: Bond length comparison of the aromatic bonds in the metal-coordinated salicylates to the corresponding bonds in free salicylic acids. Differences in bond length (Λ) are defined as $\frac{\Delta}{\sigma}$ where $\Delta(\text{Å}) = |i-j| - |C(1)-C(2)|$ and $\sigma(\text{Å}) = \sqrt{\sigma_i^2 + \sigma_j^2}$.

Λ	C(1)-C(2)	C(2)-C(3)	C(3)-C(4)	C(4)-C(5)	C(5)-C(6)	C(6)-C(1)
MnSal (_1)	0.2	0.7	-3.9	-3.7	-0.3	-4.3
MnSal (_2)	-10.3	-10.8	1.5	-5.0	7.5	-7.6
ZnSal	-13.6	-3.8	0.8	-0.9	6.0	-6.0

3.5 Conclusions

The complexes of Mn(II) salicylate dihydrate and Zn(II) salicylate dihydrate were synthesised and their structures were analysed by means of X-ray crystallography.

For both structures, a topological analysis revealed detailed information about aromatic bond lengths and strengths. In both complexes, salicylate is coordinated to the metal via the carboxylate group. This is different from the situation in SDO, where the coordination happens via both the hydroxyl- and the carboxylate-O atoms. The different coordination mode will likely influence the potential metal coordination effect and may not represent the metal-coordination effects of iron in SDO.

The observed change in the C(1)-C(2) bond length between free salicylic acid and Zn(II) salicylate dihydrate is similar to the equivalent bond length difference between the two ligands in Mn(II) salicylate dihydrate. Therefore, the difference in bond length can not be attributed to metal coordination effects. The Laplacian values ($\nabla^2\rho(r)$) at the bond critical points are not consistent with the bond lengths and are therefore not considered suitable for a bond strength comparison.

Additional high-resolution crystal structures will be necessary to make any more conclusive statements about metal coordination effects. These structures would ideally be of metal(II) salicylate complexes in which salicylate is chelated to the metal via both the hydroxyl and the carboxylate group.

4 Iron(III) salicylate dihydrate[1]

4.1 Abstract

In this contribution we present the first crystal structure of iron(III) salicylate without additional counterions. The octahedral complex contains two salicylate and two water molecules as ligands. One salicylate is mono-anionic while the other is di-anionic. Because of the centrosymmetry of the complex, the acidic hydrogen atom is disordered on the midpoint between two salicylate oxygens. The structure determination of the tiny crystal indicates the presence of reticular twinning. The structure solution of the twin is shown and an explanation based on the crystal packing is provided.

4.2 Introduction

Iron salicylates [15] and catecholates [1] play an important role in the study of non-heme iron enzymes. In these biological systems the oxidation state of iron can be easily changed which makes them catalytically interesting. In pharmaceutical sciences salicylic acid has been proposed as a chelator for iron [34]. Another important application of the salicylate ligand is in analytical chemistry. Fe(III) salicylate is a colored complex which can be used for spectrophotometry [35, 36]. Spectrophotometric procedures have also been used to establish the stability constants of Fe(III) salicylates [37]. Alternatively, the stability constants can be determined using potentiometric titrations [38, 39, 40, 41]. In the course of such experiments, different complex structures and compositions have been proposed but to our knowledge none of them has been characterized by a crystal structure analysis. We therefore set out to crystallize Fe(III) salicylate and succeeded

[1] J. A. van der Horn, B. Souvignier, and M. Lutz, "Crystallization, Structure Determination and Reticular Twinning in Iron(III) Salicylate: Fe[(HSal)(Sal)(H_2O)$_2$]," *Crystals*, vol. 7, art. 377, 2017 [33]

using the gel crystallization technique. The starting salt was Fe(II) nitrate which slowly oxidized during the reaction with salicylic acid.

4.3 Synthesis and crystallization

For the crystallization iron(III) salicylate dihyrate we used the gel technique of Arend and Connelly [32]. 6.26 g $FeSO_4 \cdot 7H_2O$ was dissolved in 40.5 mL H_2O, which resulted in an orange solution. The solution was filtered, leaving a green-blue filtrate. 4.5 mL Tetramethoxysilane was added to the solution under stirring. Stirring was continued for fifteen minutes. The mixture was poured into a test tube and left to solidify for four days. The top layer had turned yellow and was subsequently removed. 0.9 Sodium salicylate was dissolved in 10 mL of H_2O (pH $\approx$ 5.5). The solution was brought onto the gel. After five days, microcrystalline material had formed at the surface of the gel. One crystal ($25 \times 25 \times 125$ μm^3) was selected for the single crystal diffraction experiment.

4.4 X-ray crystal structure determination

X-ray intensities were measured on a Bruker Proteum diffractometer with rotating anode generator, Helios optics, and PLATINUM-135 CCD detector. A total of 1633 images was collected with a detector distance of 60 mm, a rotation increment of 0.5°/frame, an exposure time of 120 s/frame, and a generator setting of 45 kV / 60 mA. First attempts to index the reflections with the DIRAX software [42] suggested an orthorhombic C-centered unit cell (see Section 4.7). A single orientation matrix is sufficient to integrate all reflections. Space group determination and structure solution using this symmetry failed.

Therefore the intensity integration was repeated using the monoclinic subgroup with a P lattice (c = 37.57 Å). Again, only one orientation matrix was used for the integration. A twin matrix of (-1 0 0 / 0 -1 0 / 1 0 1) was included for the structure solution with the program SHELXD [43] in space group $P2_1$. With this matrix all reflections are overlapping (*pseudo*-merohedral twin). This gave a suitable starting model which could be completed by difference Fourier maps in the SHELXL software [21] based on the same twin matrix and space group.

The ADDSYM routine of the PLATON software [44] found additional translation symmetry resulting in a subcell with space group $P2_1/n$ (c = 18.79 Å). This prompted us to re-integrate the reflection data in this subcell with two orientation matrices using the Eval15 software [18]. The two orientation matrices can be related by a twofold rotation about uvw = [100] which corresponds to the matrix (1 0 0 / 0 -1 0 / -0.5 0 -1) (Scheme 7). By a twofold rotation about the monoclinic b-axis this is equivalent with a twofold twin rotation about hkl = (001) in reciprocal space and the twin matrix (-1 0 0 / 0 -1 0 / 0.5 0 1). The latter relation was used for the intensity integration. Scaling, absorption correction and merging of symmetry equivalent reflections were performed with Twinabs [45]. Because of the tiny size, the crystal did not diffract further than $\frac{\sin\theta}{\lambda}$ = 0.51 Å^{-1}. This cut-off is based on the merging R-value in the outer resolution shell. The non-overlapping reflections of the major twin component and the overlapping reflections of both twin components were stored in HKLF5 format [46] for the structure refinement.

Non-hydrogen atoms were refined freely with anisotropic displacement parameters. The rather low resolution of the data leads to a quite poor data/parameter ratio of 6.7. Consequently, all displacement parameters were restrained using the RIGU instruction [47]. C-H hydrogen atoms were introduced in calculated positions and refined with a riding model. The O-H hydrogen atom was located on position $(\frac{1}{2}, 1, 0)$ and kept fixed during the refinement. Further experimental details are given in Table 12.

Table 12: Measurement details

Molecular formula	$Fe[(C_7O_3H_5)(C_7O_3H_4)(H_2O)_2]$	
Formula weight	365.09	
Temperature	110(2) K	
Wavelength	1.54184 Å (CuKα)	
Crystal system, space group	Monoclinic, $P2_1/n$	
Unit cell dimensions	$a = 7.3392(11)$	
	$b = 4.8493(6)$	$\beta = 96.090(9)^\circ$
	$c = 18.794(3)$	
Volume	665.11(15) Å^3	
Z, Calculated density	2, 1.823 g/cm^3	
Absorption coefficient	9.53 mm^{-1}	
F(000)	374	
Crystal size	$25 \times 25 \times 125$ μm^3	
$(\frac{\sin\theta}{\lambda})_{max}$	0.51 Å^{-1}	
Limiting indices	-7 $\leq h \leq$ 7	
	-4 $\leq k \leq$ 4	
	-18 $\leq l \leq$ 19	
Refl. collected / unique / observed	3505 / 1246 / 1033	[R_{int} = 0.0574]
Completeness to $\theta = 51.35^\circ$	99.0%	
Number of parameters	107	
Number of restraints	93	
R1/wR2 [$I > 2\sigma(I)$]	0.0678 / 0.1730	
R1/wR2 [all refl.]	0.0862 / 0.1901	
Goodness of Fit	1.073	
Twin fraction (BASF)	0.461(4)	
Residual density [min/max]	-0.48 / 0.71 eÅ^{-3}	

4.5 Intramolecular interactions

Compound **1** (Scheme 5) crystallizes in the monoclinic space group $P2_1/n$ with the Fe atom on an exact, crystallographic inversion centre (Wyckoff position c). It is hexacoordinated by oxygen atoms originating from two salicylato and two aquo ligands, respectively. The geometry of the FeO_6 polyhedron is octahedral with only a very slight deviation from perfect O_h symmetry. This deviation can be expressed by a quadratic elongation of 1.003 and an angular variance of 1.42 deg^2 [48]. Considering the complete complex we find an approximate C_{2h} symmetry with an r.m.s. deviation of 0.0276 Å[49]. In the octahedron the equatorial plane is formed by two symmetry equivalent salicylato ligands which coordinate as chelate in bidentate fashion. The salicylate molecule is essentially planar with a maximum torsion angle of 2.7(7)° in the six-membered chelate

ring. The axial positions of the octahedron are occupied by water molecules. The plane of the water molecule forms an angle of 30° with the water-Fe bond. This is halfway between a trigonal and a tetrahedral coordination mode. A molecular plot of the structure is shown in Figure 18.

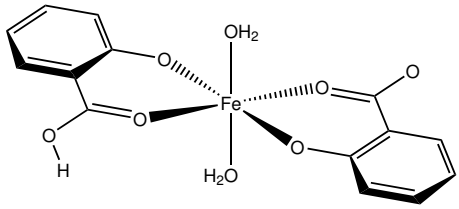

Scheme 5: Molecular structure of compound **1**.

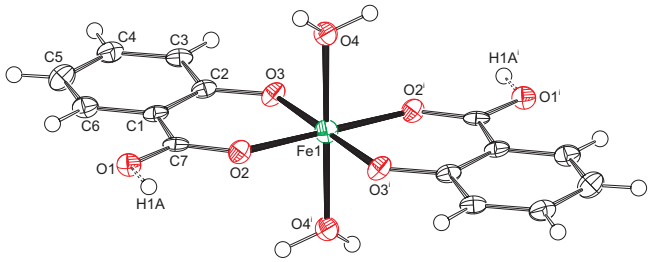

Figure 18: Displacement ellipsoid plot of compound **1**. Ellipsoids are drawn at the 50% probability level. Hydrogen atoms are drawn as small spheres with arbitrary radii. Atoms Fe1 and H1A are located on special positions. Consequently, only half of the O1 atoms are protonated. Symmetry code $i : -x, 1-y, -z$.

The Fe-O distances to the salicylate ligand are 1.925(6) and 1.973(6) Å and to the water molecule 2.092(6) Å. A comparison of these values with the literature [50, 51] indicates that the iron must be in oxidation state +3. Bond-valence calculations [52] result in a bond-valence sum of 3.206 [44] confirming this oxidation state. With an oxidation state +3 for the iron, one of the two salicylate ligands must be protonated for charge balance. From steric considerations protonation should take place at O1 which is the only oxygen not coordinated to the iron. Inspection of the intermolecular contacts indeed shows a short $O1 \cdots O1^i$ distance of 2.476(8) Å that can only be explained by the presence of a hydrogen bond (symmetry code $i : 1-x, 2-y, -z$). We therefore introduced a hydrogen atom on the midpoint between O1 and $O1^i$ which is a special position (Wyckoff position *d*). With both Fe1 and H1A on special positions the charge balance is achieved for a Fe(III) complex with the formula $[Fe(HSal)(Sal)(H_2O)_2]$. With this description the O1-H1A distance becomes rather long (1.24 Å). More likely is an alternative explanation as double-well hydrogen bond. Such double-well potentials preferably occur in very strong and stabilized hydrogen bonds [53, 54]. A difference Fourier map at the position of H1A gives some indication for a double-well situation (Figure 19) but due to the weak diffraction of the crystal and the twinned reflection data this is not a full proof. For convenience we left the hydrogen atom unrefined on the special position.

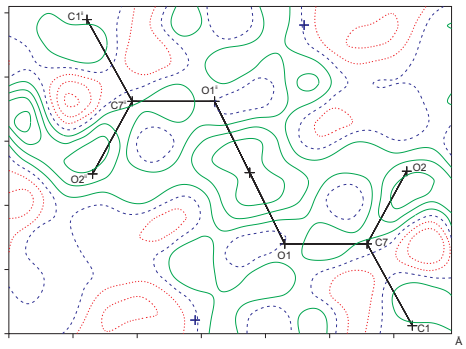

Figure 19: Difference Fourier map in the C7-O1-O1^{ii} plane as calculated with the PLATON software [44]. The observed structure factors F_o^2 were de-twinned with SHELXL (instruction LIST 8) [21]. Hydrogen atom H1A was omitted in the calculation of F_c^2. Contour level 0.1 e/Å^3. Positive contours are drawn in green, negative contours in red, and the zero contour in blue. Symmetry code $ii: 1-x, 2-y, -z$.

Salicylic acid (2-hydroxybenzoic acid, H_2Sal) is a di-basic acid with pK_a values of 2.853(9) and 12.897(7) [55, 56]. Metal complexes of the mono-anionic ligand $HSal^-$ are well known from the literature. For recent examples of transition metal complexes, see [57, 58, 59, 60]. In the majority of cases the hydroxyl group is protonated and the carboxylate group deprotonated. The carboxylate group can then act as monodentate, bidentate or bridging moiety. In total 339 metal complexes of this kind are known in the Cambridge Structural Database [61]. It is very rare that the carboxylate group is protonated and the hydroxyl group deprotonated (Scheme 6). Coordination mode (I) is found in a Cu complex [62] and mode (II) in Ag compounds [63]. Coordination mode (III) of the present study has been first described for a MoO_2 complex [64] and more recently in a Cu complex [65]. In total five crystal structures with coordination mode (III) are known in the Cambridge Structural Database (update November 2016) [61] with determined atomic coordinates. Interestingly, all five complexes show a non-symmetric pattern with both $HSal^-$ and Sal^{2-} in the coordination environment. In all five structures the metal complex is located on a general position with C_1 symmetry. Compound **1** of the present study also has both $HSal^-$ and Sal^{2-} in the coordination environment but as a consequence of the crystallographic C_i symmetry the ligands are non-distinguishable. While the Cu complex [65] is also described with a symmetric $O-H\cdots O$ hydrogen bond, compound **1** of the present study is the first molecule with the metal centre and H1A on special positions.

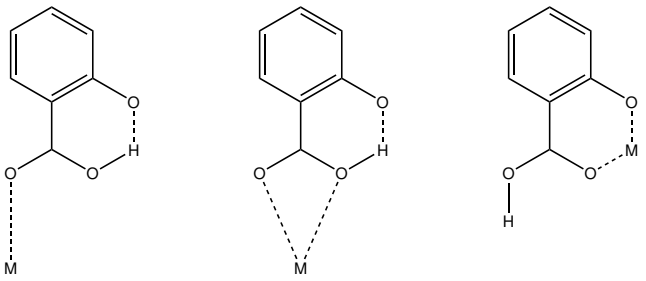

Scheme 6: Coordination modes of mono-anionic $HSal^-$ where the carboxyl group is protonated and the hydroxyl group deprotonated.

From the statistical analysis of the crystal structures with the $HSal^-$ ligand it is clear that the carboxylate group is much easier deprotonated (339 cases) than the hydroxyl group (7 cases in modes I, II and III). Why do the structures with deprotonated hydroxyl group exist at all? The answer might be in the very strong intermolecular hydrogen bond in the crystal [66]. Indeed, the hydrogen bonded $O \cdots O$ distance in compound **1** is very short (2.476(8) Å). This is generally the case in the $HSal^-$ structures with deprotonated hydroxyl group. This intermolecular effect might thus be the reason for the increased thermodynamic stability.

4.6 Intermolecular interactions

The molecules of compound **1** are connected by hydrogen bonds with the protonated carboxylate group and the coordinated water molecules as hydrogen bond donors. The non-coordinated carboxylate oxygen O1 and the deprotonated hydroxyl group act as acceptors (Table 13). This hydrogen bonding pattern results in a two-dimensional network parallel to the a, b-plane (Figure 20). No strong intermolecular interactions could be detected in c-direction, which leaves as only possibility weak dispersive effects in this direction.

Table 13: Hydrogen bonding interactions in compound **1**. Symmetry codes $i : 1-x, 2-y, -z$; $ii : x-1, y, z$; $iii : x, y+1, z$

$D-H\cdots A$	$D-H$	$H\cdots A$	$D\cdots A$	$D-H\cdots A$
$O1-H1A\cdots O1^{i}$	1.24 Å	1.24 Å	2.476(8) Å	180°
$O4-H4A\cdots O1^{ii}$	0.95 Å	1.87 Å	2.808(8) Å	170°
$O4-H4B\cdots O3^{iii}$	0.95 Å	1.81 Å	2.704(9) Å	156°

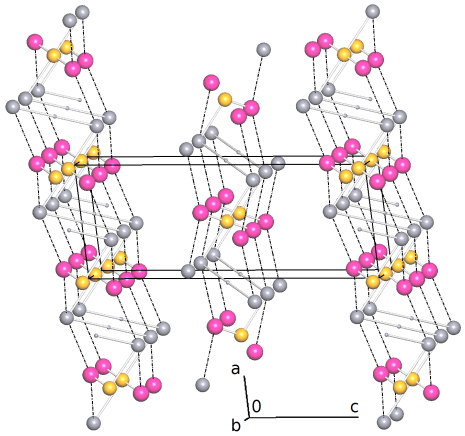

Figure 20: Simplified net calculated with ToposPro [67]. Large gray spheres represent the nodes of Sal^{2-}, pink spheres H_2O and yellow spheres Fe^{3+}. The O-H hydrogen atoms on special positions are drawn as small gray spheres. Coordinative Fe-O bonds are drawn as sticks and hydrogen bonds are drawn as dashed lines.

4.7 Reticular twinning

The reflection data can be indexed with a C-centered orthorhombic symmetry (a = 7.24 Å, b = 74.79 Å, c = 4.85 Å). Concerning the X-ray intensities, the merging R values for this symmetry are reasonably low. Investigation of the systematic absences indicates space group $C222_1$ but there is an additional *pseudo* B-centering present. A closer inspection of the reflection data shows that this *pseudo* B-centering is caused by the presence of additional (non space group compatible) systematic absences: in the layers of $h = 2n$ only reflections with $h + k = 4n$ are present. Structure solution in space group $C222_1$ failed.

Because systematic absences incompatible with space group symmetry are a clear warning sign for twinning [68], we decided to select a primitive subgroup with monoclinic symmetry and a = 7.34 Å, b = 4.85 Å, c = 37.57 Å, β = 95.6° (Scheme 7). Based on the metric orthorhombic symmetry, a twofold rotation about the a axis was chosen as a potential twin operation. Systematic absences indicated space group $P2_1$. But also in this setting there are absences incompatible with the space group: in the layers of $h = 2n$ all reflections with l = odd are absent (Figure 21). Structure solution as a twin in space group $P2_1$ was successful (see Experimental Section). There are two independent molecules in the asymmetric unit which are both located on general positions with C_1 symmetry.

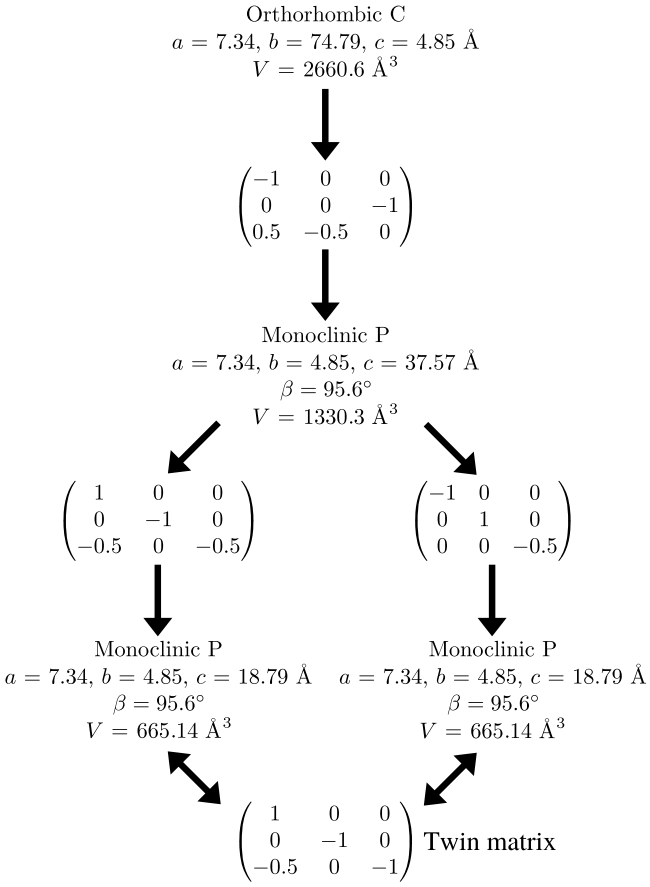

Scheme 7: Supercell decomposition

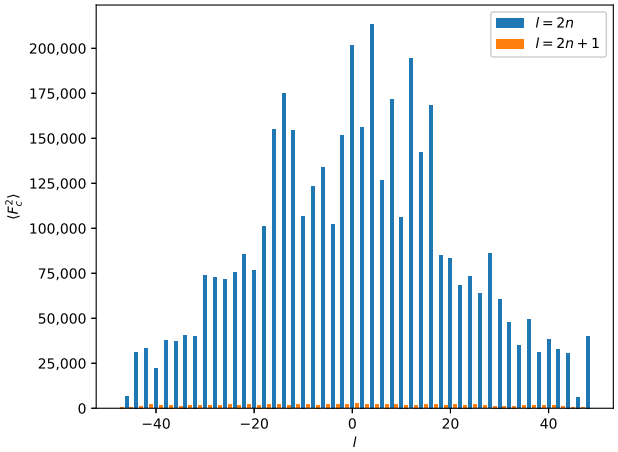

Figure 21: Average F_c^2 for a perfect twin in the $P2_1$ supercell for reflections with $h = 2n$. The l-index is shown on the x-axis. Reflections with $l = 2n + 1$ are absent (small orange bars). Systematic absences for a combination of $h = 2n$ and $l = 2n + 1$ are incompatible with the $P2_1$ space group.

Importing the $P2_1$ structure into the PLATON routine ADDSYM [44] finds additional translational symmetry in c direction. Halving the c axis results in the true unit cell ($a = 7.34$ Å, $b = 4.85$ Å, $c = 18.79$ Å and $\beta = 95.6°$) with space group $P2_1/n$. The relation between the $P2_1$ supercell and the $P2_1/n$ subcell can be seen in Figure 22, which also shows the stacking of the hydrogen bonded planes. Stacking faults in c-direction result in the twinned structure of the current analysis. This alternative stacking is shown in Figure 23. The stacking with true translational symmetry (Figure 22) as well as the alternative stacking with twinned symmetry (Figure 23) show no conflicting short contacts between the layers. We assume that both arrangements are energetically similar. The overlapping twin boundary is depicted in Figure 24 and shows an additional, approximate symmetry operation $(x+1/2, y+1/2, 1/2-z)$ which is a combination of the n-glide plane of the space group and the twin rotation about a. Twin generation by stacking faults have previously been discussed by Dornberger-Schiff in the context of the OD-theory [69].

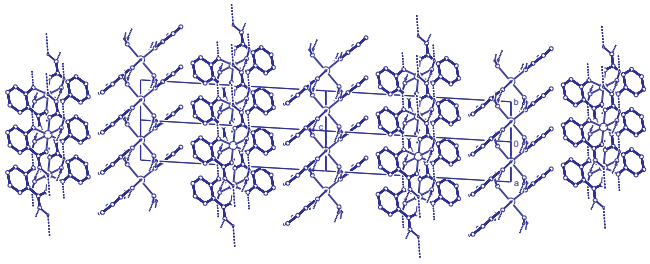

Figure 22: Stacking of the hydrogen bonded layers. Projection along the $uvw = [110]$ direction. Two unit cells of the $P2_1/n$ structure are shown. This doubled cell corresponds to the $P2_1$ supercell described in the text. C-H hydrogen atoms are omitted for clarity.

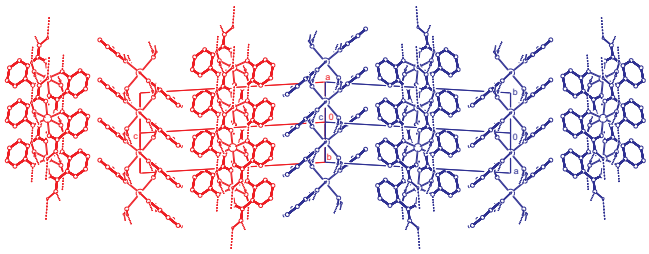

Figure 23: Alternative stacking of the hydrogen bonded layers. Projection along the $uvw = [110]$ direction. The red and blue unit cells ($P2_1/n$ setting) are related by the twin operation about c^*. C-H hydrogen atoms are omitted for clarity.

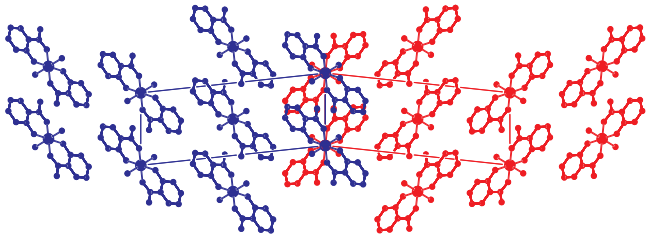

Figure 24: View on the twinned structure along the $uvw = [010]$ direction ($P2_1/n$ setting). The second unit cell is generated by the twin operation about a. At the twin boundary both components are drawn. The blue molecules are related to the red molecules by an approximate operation $x + 1/2, y + 1/2, 1/2 - z$. This operation is not part of the $P2_1/n$ space group but is obtained by a combination of the n-glide $x + 1/2, 1/2 - y, z + 1/2$ and the twin operation (rotation) about a: $x, -y, -z$. Hydrogen atoms are omitted for clarity.

Figure 25 and Figure 26 show the direct and reciprocal lattice for this reticular twin. Figure 26 clearly shows that the twinning is the reason for space group incompatible absences. With the knowledge of the true unit cell size and true twin relation it is possible to freely refine the cell parameters. Based on the non-overlapping reflections of the first twin component, this results in $a = 7.3392(11)$ Å, $b = 4.8493(6)$ Å, $c = 18.794(3)$ Å and $\beta = 96.090(9)°$. With these values the twin obliquity is 0.49° as calculated with PLATON using the LEPAGE-twin algorithm [70].

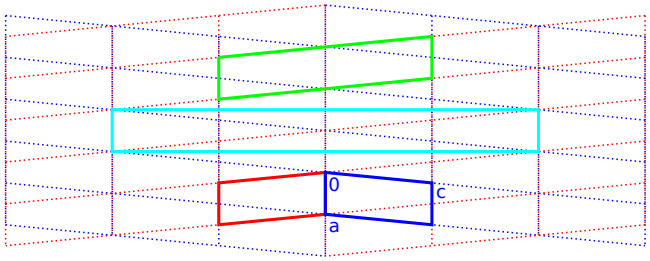

Figure 25: Direct lattice of the unit cell as described in Table 12, viewed in the ac plane. Blue and red indicate the individual unit cells ($P2_1/n$ setting). Green and cyan, respectively, indicate monoclinic-P and orthorhombic-C twin supercells. The blue and red lattices are derived from the monoclinic superlattice (see Scheme 7).

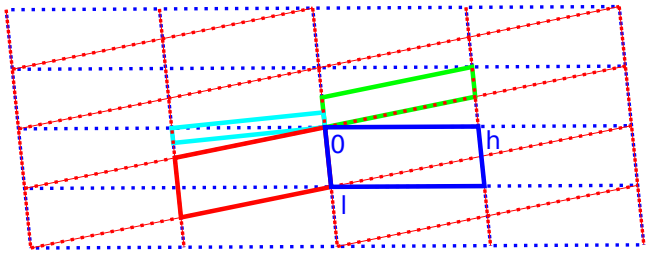

Figure 26: Reciprocal lattice of the unit cell as described in Table 12, viewed in the $h0l$ plane. Blue and red indicate the individual unit cells ($P2_1/n$ setting). Green and cyan respectively indicate monoclinic-P and orthorhombic-C twin supercells. The blue and red lattices are derived from the monoclinic superlattice (see Scheme 7).

4.8 Conclusions

The octahedral complex molecules of $Fe[(HSal)(Sal)(H_2O)_2]$ are connected by intermolecular hydrogen bonds to form layers in the a, b-plane. Stacking faults in the c-direction lead to the reticular, pseudo-orthorhombic twinning. The twin matrix was obtained by decomposition of the C-centered orthorhombic twin cell as (1 0 0 / 0 -1 0 / -0.5 0 -1). This corresponds to a twofold rotation about the monoclinic a-axis. Two orientation matrices were used for the determination of the X-ray intensities. In every second layer in h-direction the reflections of both twin domains fully overlap, while in the odd layers the reflections are separated. This situation is characteristic for reticular twinning. Taking this twinning situation into account, the chemistry of the complex can be consistently explained. The oxidation state of the Fe was determined as +3, and the O-H hydrogen atom is on the intermolecular midpoint between two carboxylate oxygens.

5 Triethanolaminato iron(III) salicylate

5.1 Introduction

After successful synthesis and crystallization of *iron(III) salicylate dihydrate* (chapter 4), we set out to crystallize a similar complex with an additional, stabilizing tetradentate ligand. As the Fe-atom in the catalytic centre in SDO is coordinated by three histidine side chains, this could potentially create a more realistic catalytic environment for the iron atom in our model compound. As inspiration for the synthesis of our new complex, the complex of *triethanolaminato Mn(III) salicylate* (Scheme 8) was used, as described by Langley et al. [31] This complex features a coordinated nitrogen atom and may provide a first step towards a proper biomimetic complex. Based on this paper, we designed a synthesis procedure for *triethanolaminato iron(III) salicylate*. No such complex has been described in the literature. Several iron complexes with triethanolamine as a ligand are known from the literature and will be used for comparison. [71, 72, 73, 74, 75, 76, 77, 78, 79, 80, 81, 82, 83]

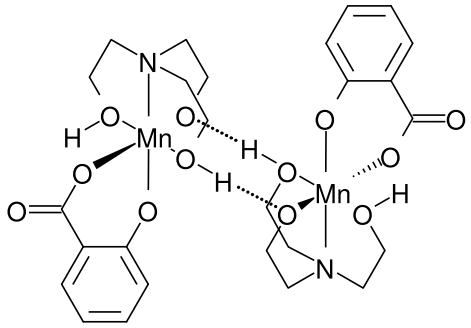

Scheme 8: Molecular structure of triethanolaminato manganese(III) salicylate ($Mn[C_6H_8O_3N][C_7H_4O_3]$) as determined by Langley et al. [31]

5.2 Synthesis and crystallization

0.12 g Salicylic acid was dissolved in 5 mL of methanol and added to a solution of 0.28 g $FeSO_4 \cdot 7H_2O$ in 5 mL MeOH. Hereto was added 0.13 mL of triethanolamine and 0.70 mL of triethylamine whilst stirring. A vapour diffusion crystallization experiment was setup from the resulting solution with diethylether as the antisolvent. After 4 days, small needle-shaped crystals had formed, suitable for X-ray diffraction.

5.3 X-ray crystal structure determination

Data was collected at 110 (2) K. Peaks were indexed with the Saint software [84] in the monoclinic P unit cell and integrated with Eval15 [85]. Absorption correction and scaling was done in SADABS. [19] The structure was solved with SHELXT in space group $P2_1/n$ and was found to be highly disordered. [20] Refinement was done in SHELXL. [21] Disorder in the structure was modeled with the PART command and/or restrained with the ISOR and RIGU commands in SHELXL. All salicylate ligands were restrained with the SAME command.

All triethylamine $N-C$ and $C-C$ bonds as well as $N-C-C$ and $C-N-C$ angles were restrained with the SADI command. Non-modeled solvent density was covered with the SQUEEZE [86] utility in PLATON. [44] A total of 358 electrons within a solvent accessible volume of 1238 Å^3 were *squeezed*. Additional experimental details can be found in Table 14.

Table 14: Experimental details for triethanolaminato iron(III) salicylate

Molecular formula	$(Et_3NH)_3 \cdot Fe_4(Sal)_6(tea)$ + disordered solvent
Formula weight	1492.77 [a]
Temperature	110(2) K
Wavelength	0.71073 Å (MoKα)
Crystal system, space group	Monoclinic, $P2_1/n$ (14)
a, b, c	30.1559(14), 17.0281(9), 30.9103(13) Å
β	115.309(2)°
Volume	14348.9(12) Å^3
Z, Calculated density	8, 1.382 g/cm^3 [a]
Absorption coefficient	0.866 mm^{-1} [a]
F(000)	6240
$(\frac{\sin\theta}{\lambda})_{max}$	0.61 Å^{-1}
Limiting indices	-36 $\leq h \leq$ 36
	-20 $\leq k \leq$ 20
	-37 $\leq l \leq$ 37
Refl. collected / unique / $I \geq 2\sigma(I)$	199964 / 26725 / 13687 [R_{int} = 0.1515]
Completeness to $\theta = 25.501°$	100%
Number of parameters	1873
Number of restraints	3705
R1/wR2 [$I > 2\sigma(I)$]	0.0746 / 0.1793
R1/wR2 [all refl.]	0.1591 / 0.2224
Goodness of Fit	1.019
Residual density [min/max]	-0.907 / 1.989 eÅ^{-3}

[a] Derived values do not contain the contribution of the disordered solvent.

Although the crystal structure of *triethanolaminato iron(III) salicylate* (Scheme 9) was successfully solved in space group $P2_1/n$, uncertainty remains in the space group determination. Distinct similarities were found in the disordered parts of both anions, which may be explained by incorrect space group symmetry. Analysis of reflection data with the program Superflip [87] suggests the presence of the following symmetry elements: n glide plane (agreement factor 0.611%), 2_1 screw axis (agreement factor 7.198%) and inversion (agreement factor 7.838%). The agreement factor measures the *degree of coincidence*, where a random operation should result in an agreement factor of 100%. Even though space group $P2_1/n$ is recommended by the program, the analysis shows a stronger agreement of the n glide plane with the data as compared to the 2_1 screw axis and the inversion symmetry element. The reflection statistics in our data (see below) indicate a hypercentric crystal structure [88], which leaves the matter of centrosymmetry versus non-centrosymmetry of the structure undecided. [89] Structure solution in space group Pn turned out successful and showed no disorder in the initial model. However, refinement in this space group was unstable due to very high

($> 90\%$) correlation matrix elements. Space group $P2_1/n$ is used for the rest of the analysis.

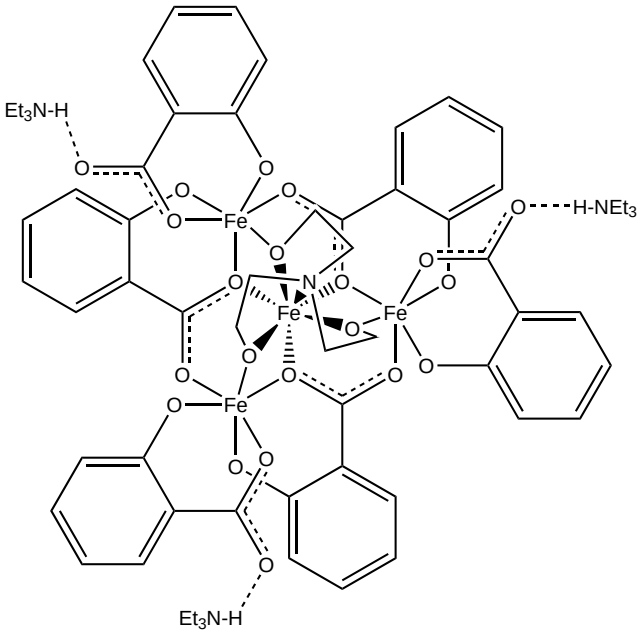

Scheme 9: Molecular structure of triethanolaminato iron(III) salicylate in the crystal

5.4 Crystal structure

The asymmetric unit consists of two anionic iron complexes, six triethylammonium moieties and various solvent molecules. The anion complexes each contain four iron centres (one central and three noncentral) which are coordinated by six salicylate ligands and one triethanolamine ligand. Apparent *pseudo*-threefold rotation symmetry at the central iron atoms is present in the anion complexes. (Figure 27) This is confirmed by the MOLSYM utility in PLATON [44] when applied to all O, N and Fe atoms, showing a maximum deviation of 0.22 Å from C_3 symmetry in both complexes. Reflection statistics obtained from the program Sir2014 [90] show an average value of $|E^2 - 1| = 1.287$, indicating hypercentricity in the crystal. [88] Hypercentric crystals are known to incorporate *pseudo*-translational symmetry. [89] A search for *pseudo*-translational symmetry [91] in reciprocal space was done with the program Sir2014 [90] and revealed the relation $2h + k = 4n$.

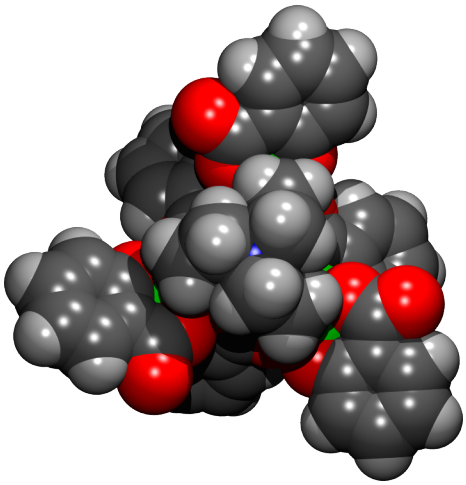

Figure 27: POV-Ray view of the anion along the *b*-axis generated by PLATON [44], showing near C_3 symmetry

The six salicylate ligands in the anion exist in two distinct coordination modes, shown in Scheme 10. Each anion complex contains three salicylate ligands with coordination mode **1** and three with coordination mode **2**. Disorder in the salicylate ligands was only found in the ligands with coordination mode **1**.

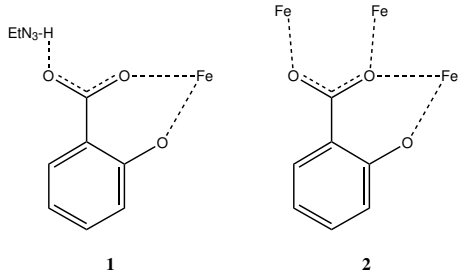

Scheme 10: Coordination modes of salicylate in the anion complex

Both anion complexes as well as all triethylammonium ligands were incorporated in the final model. (Figure 28) Although the overall structure was quite well defined, a split molecule model was used for the most disordered salicylate ligand and triethylamine molecules.

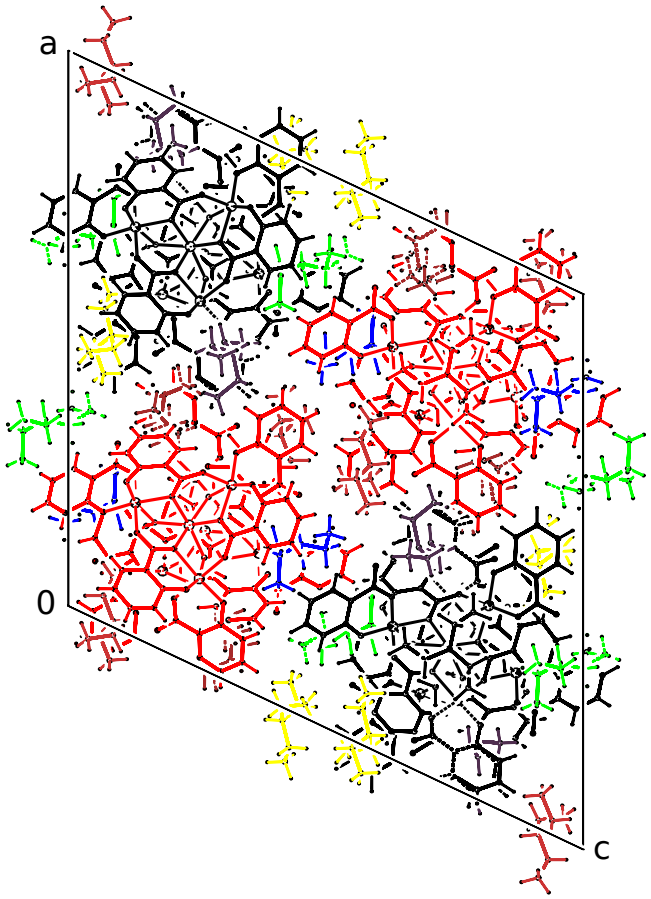

Figure 28: Packing of anions and cations in the unit cell. Symmetry related residues are colored equally.

All triethylamine N-atoms are in close proximity of a carboxylic O-atom (2.554 - 2.836 Å), suggesting the presence of hydrogen bonds. Shallow residual peaks were indeed found near some of the triethylamine N-atoms and therefore N-H hydrogens were introduced on all triethylamine molecules. The resulting hydrogen bonds can be found in Table 15. No O-H hydrogen atoms were found on any of the ligands. This is confirmed by the absence of potential hydrogen bond acceptors and the total charge balance, which is discussed below.

Table 15: Hydrogen bonds present in the structure (symmetry codes i: $-\frac{1}{2}+x, \frac{1}{2}-y, -\frac{1}{2}+z$; ii: $\frac{3}{2}-x, \frac{1}{2}+y, \frac{1}{2}-z$; iii: $\frac{1}{2}-x, \frac{1}{2}+y, \frac{1}{2}-z$)

$D-H\cdots A$	$D-H$ (Å)	$H\cdots A$ (Å)	$D-A$ (Å)	$D-H\cdots A$ (°)
N13 - H13 $\cdots$ O71^{i}	1.00	1.65	2.649(8)	173
N14 - H14 $\cdots$ O72	1.00	1.68	2.670(9)	170
N15 - H15 $\cdots$ O13A$^{ii\ a}$	1.00	1.74	2.604(12)	143
N15 - H15 $\cdots$ O13B$^{ii\ a}$	1.00	1.85	2.838(12)	169
N16 - H16 $\cdots$ O132^{iii}	1.00	1.62	2.554(10)	153
N17 - H17 $\cdots$ O11^{ii}	1.00	1.60	2.580(10)	164
N18E^{a}- H18E$^{a}\cdots$ O12^{iii}	1.00	1.74	2.710(10)	163

[a]Disordered atom position

The crystal structure contains large voids (1238 Å^3/ unit cell) filled with disordered methanol and water solvent molecules. Their contribution to the structure factors was secured by back-Fourier transformation using the SQUEEZE algorithm [86] resulting in 358 electrons / unit cell. The displacement ellipsoid plot of the anions in the final model shows a high uncertainty in the atom positions. (Figure 29)

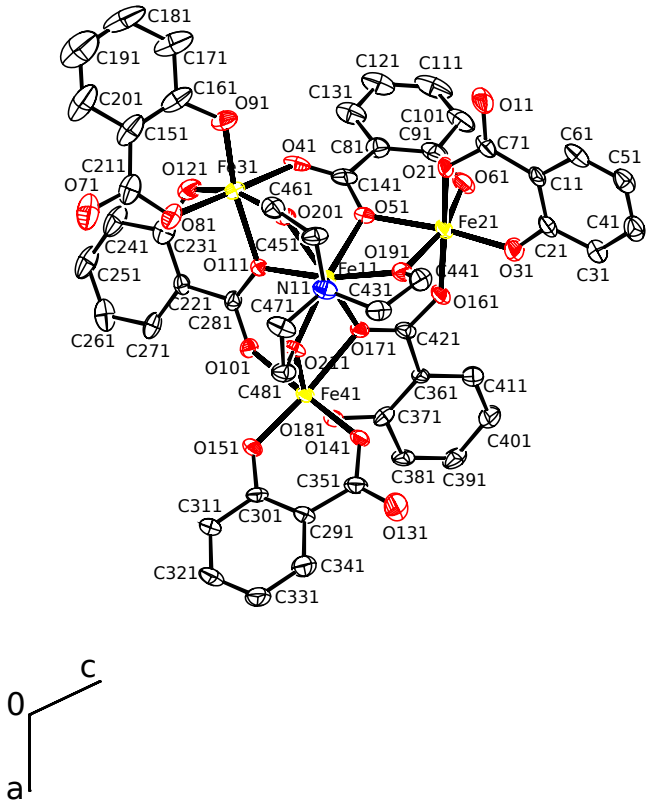

Figure 29: Displacement ellipsoid plot of the anion drawn at 50% probability. Hydrogen atoms, triethylammonium cations, unresolved solvent molecules and the second anion are omitted for clarity.

The large amount of disorder and unresolved solvent density may be partly attributed to the weak reflection data. Of the 26725 unique reflections, only 13687 (51%) are observed ($I \geq 2\sigma(I)$). Figure 30 shows an impression of the situation in the reciprocal space, indicating the weak reflection data.

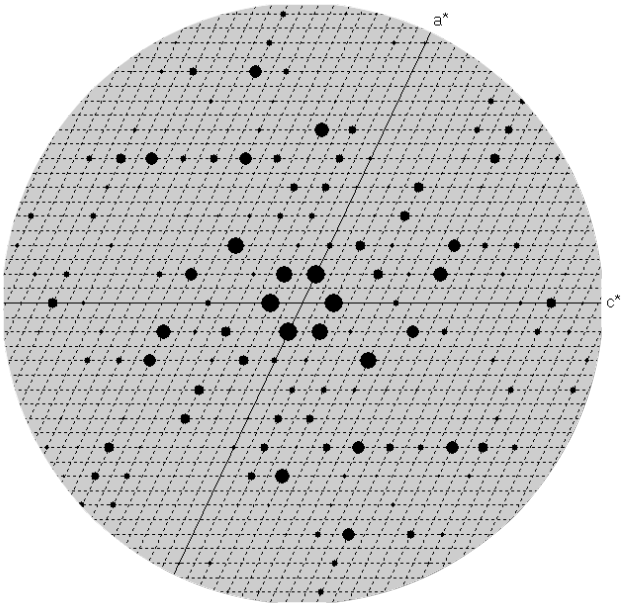

Figure 30: Simulated precession image of merged reflections in the $h0l$ plane, generated from experimental reflection data with the program *LAYER*. [92] Relative reflection intensities are represented by size of spheres.

With Fe^{II} as a starting material, it is interesting to know whether the oxidation states of the iron atoms have changed or not, as this may affect the geometric parameters of the coordinated ligands. Even though there are 8 crystallographically independent iron atoms in the assymetric unit, it appears that there are only two chemically different types of iron centres. The two types will be addressed individually, as they do not necessarily have the same oxidation state. Various examples exist in literature of mixed-valence iron complexes, in which some of the iron atoms have oxidation state +2 whereas others have +3. [71, 93, 94, 95, 96]

To determine the iron oxidation states, a bond-valence sum calculation [52] was done with PLATON [44] on all iron atoms. For the central iron atoms Fe11 and Fe12, the bond-valence sums were found to be 2.825 and 2.870, respectively. For all surrounding iron atoms, the values are in the range 3.190 - 3.242. These calculations lead to believe that the all iron atoms have oxidation state +3. However, the relatively large gap between the calculated oxidation states for the different types of iron centres still leaves room for discussion.

To gain more insight in the oxidation state of the central iron atom, a literature search was done in the Cambridge Structural Database (2016) [97] for iron atoms with a three- or fourfold coordinated triethanolamine ligand. A total of 28 different crystal structures was found. In all corresponding articles,

these iron atoms are reported to be in oxidation state +3 and without any O-H hydrogen atoms on the triethanolamine ligands. [71, 72, 73, 74, 75, 76, 77, 78, 79, 80, 81, 82, 83] Fe-O bonds were found to be in the range 1.872 - 2.184 Å for trietylamine oxygen atoms and 1.872 - 2.313 Å for all coordinating oxygen atoms. Fe-N bond lengths are in the range of 2.144 - 2.37 Å. Nonbonded triethylamine-N atoms are found at a distance between 2.467 and 3.034 Å to iron. These data correspond with our findings. (Table 16) In chapter 6 the structure of triethanolaminato iron will be discussed, where the triethanolamine ligand turns out to be singly protonated and coordinated to Fe^{II} instead of what was originally reported [71].

With a charge distrubtion of +3 for the noncentral iron atoms (6x), -2 for salicylate (12x), -3 for triethanolamine (2x) and +1 for triethylamine (6x), one can reasonably assign an oxidation state of +3 for to the central iron atoms (2x), resulting in the overall formula being $(Et_3NH^+)_3 \cdot Fe_4^{III}(Sal^{2-})_6(tea^{3-})$, assuming no charged molecules have been discarded with the SQUEEZE procedure.

Table 16: Selected bond lengths (Å) and angles (°) from the anions. Atoms in bold belong to triethanolamine.

Fe11 - **O191**	1.960(5)	Fe21 - O21	1.992(5)	Fe12 - **O192**	1.947(4)	Fe22 - O22	2.006(4)
Fe11 - **O201**	1.965(4)	Fe21 - O31	1.896(5)	Fe12 - **O202**	1.964(4)	Fe22 - O32	1.906(5)
Fe11 - **O211**	1.963(4)	Fe21 - O61	1.932(5)	Fe12 - **O212**	1.959(4)	Fe22 - O62	1.931(5)
Fe11 - O51	2.259(4)	Fe21 - O51	2.088(4)	Fe12 - O52	2.261(4)	Fe22 - O52	2.079(5)
Fe11 - O111	2.221(4)	Fe21 - O161	2.040(4)	Fe12 - O112	2.235(4)	Fe22 - O162	2.031(4)
Fe11 - O171	2.277(4)	Fe21 - O191	2.003(5)	Fe12 - O172	2.242(4)	Fe22 - O192	2.009(5)
Fe11 - **N11**	2.259(5)			Fe12 - **N12**	2.253(6)		

X-Fe11-Y	**O191**	**O201**	**O211**	O51	O111	O171	**N11**
O191	-						
O201	112.57(19)	-					
O211	114.57(19)	117.26(18)	-				
O51	72.86(18)	83.45(17)	148.88(17)	-			
O111	152.44(18)	73.61(17)	82.63(16)	81.58(15)	-		
O171	83.09(17)	150.96(17)	73.29(16)	78.00(15)	81.67(15)	-	
N11	77.3(2)	76.5(2)	76.1(2)	133.89(19)	129.38(19)	132.18(19)	-

X-Fe21-Y	O21	O31	O61	O51	O161	O191
O21	-					
O31	89.9(2)	-				
O61	92.3(2)	98.1(2)	-			
O51	92.09(19)	174.33(19)	87.13(18)	-		
O161	177.2(2)	90.17(19)	90.47(19)	87.54(17)	-	
O191	89.6(2)	98.8(2)	162.99(19)	75.90(18)	87.60(18)	-

5.5 Conclusions

The structure of triethanolaminato iron(III) salicylate was solved and analyzed in space group $P2_1/n$, although the precise space group symmetry could not be conclusively determined. Alternative structure solution in space group Pn caused for unstable refinement of the model. The available reflection data were rather weak, which which is the consequence of a highly disordered crystal structure. Not all electron density could be modeled, leaving a solvent accessible void of 8.6% of the unit cell volume unresolved.

Two anionic four-centre iron complexes are present in the structure, which are balanced by six triethylammonium counterions. The iron atoms are coordinated by either triethanolamine or salicylate and do therefore not provide a suitable analog for the SDO catalytic site. Salicylate ligands were found in two distinct coordination modes within the complexes. The counterions are connected to the salicylate carboxylic O-atoms via $N - H \cdots O$ hydrogen bonds.

Several *pseudo*-symmetry elements are present in the crystal: two *pseudo* C_3 rotation axes through the central iron atoms in the anions and a *pseudo*-translational symmetry via the reciprocal relation $2h + k = 4n$. Based on a total charge count and a bond-valence sum calculation, the iron oxidation states were determined to be +3 for all iron centres in the structure, assuming no charged solvent molecules were overlooked.

The crystal structure is of insufficient quality for an aromatic bond length analysis of salicylate. Nevertheless, successful synthesis of this compound may provide a route towards new synthesis procedures for iron salicylate complexes.

6 Triethanolaminato iron[2]

6.1 Abstract

The X-ray crystal structure of triethanolaminato iron is known from the literature [71] in space group $I2_13$ and was re-investigated in the present study. We find a new space group symmetry of $Pa\bar{3}$ and could detect O-H hydrogen atoms which were missing in the original publication. Consequences on the Fe oxidation states are investigated with the bond-valence method resulting in a core of 4 Fe[II] and 3 Fe[III]. Symmetry relations between the two space groups and the average supergroup $Ia\bar{3}$ are explained in detail.

6.2 Introduction

The crystal structure of triethanolaminato iron is known from the literature in the non-centrosymmetric space group $I2_13$ with a unit cell volume of 10849.9(3) Å^3. [71] The composition of the cation was given as $C_{36}H_{72}Fe_7N_6O_{18}$. One Fe centre is on a threefold axis, and two are on general positions. Based on bond distances and charge balance, the original publication assigns oxidation state +2 to Fe1 and +3 to Fe2 and Fe3, respectively. The overall ratio between oxidation state +2 and +3 is then 1:6. Bond valence sum calculations were not very conclusive and the authors could not exclude a mixed valence situation. The

[2] J. A. van der Horn and M. Lutz, "Triethanolaminate iron perchlorate revisited: change of space group, chemical composition and oxidation states in $[Fe_7(tea)_3(tea\text{-}H)_3](ClO_4)_2$ (tea-H_3 is triethanolamine)," *Acta Crystallographica Section C*, vol. 74, Feb 2018. in press [98]

Fe^{II} centre is octahedrally surrounded by six oxygen atoms, and the Fe^{III} centres octahedrally by five oxygens and one nitrogen, respectively. The $Fe-O$ distances are in the range of 2.123(6) to 2.181(5) Å for Fe^{II} and 1.953(6) to 2.183(6) for Fe^{III}. In addition, there are two crystallographically independent perchlorate anions on threefold axes.

Validation with the PLATON software [44] clearly indicates the presence of an inversion centre. The program suggests a space group change from $I2_13$ to $Ia\bar{3}$ giving a 100% fit with a maximum deviation of 0.09 Å for the non-hydrogen atoms in the cation. The validation software additionally warns for short intermolecular $O-O$ distances. $O2$ and the symmetry related $O2^{i}$ are separated by 2.574(9) Å, $O5$ and $O5^{ii}$ by 2.649(9) Å (symmetry codes i: -x 1/2-y z; ii: 1/2-x y 2-z). Such short intermolecular distances strongly suggest the presence of hydrogen bonds. Because of the symmetry relations the missing O-H hydrogen atoms must be located on or disordered about special positions with an occupancy of $\frac{1}{2}$. No hydrogen atoms at these positions are given in the original publication.

As the original reflection data were not available to us, we re-synthesized the compound and performed a new X-ray diffraction experiment.

6.3 Synthesis and crystallization

Synthesis has been performed according to the literature procedure. [71] 0.26 g $Fe(ClO_4)_2 \cdot xH_2O$ (Aldrich) was dissolved in 3 mL methanol in a test tube. 3 mL Methanol was carefully layered on top of it. Afterwards, a solution of 0.53 mL triethanolamine in 10 mL methanol was slowly added on top. After two days, crystals suitable for X-ray diffraction had formed.

6.4 X-ray diffraction experiment

Peak search and indexing on the strongest reflections confirms the cubic I-centered cell of the literature. [71] Weak, non-indexed reflections in the original frames and a two-dimensional reconstruction (simulated precession image) prompted us to integrate the data in the cubic P-cell of the same volume. Data collection was performed at 100(2) K. Cell determinations at 220(2) and 293(2) K show no phase transition. The weak superstructure reflections are still present at these temperatures.

Refinement in $I2_13$ used the coordinates of [71] as starting model. Transformation to the $Ia\bar{3}$ supergroup was performed with ADDSYM in PLATON. [44] Structure solution in $Pa\bar{3}$ was performed with SHELXT [20].

A leverage analysis has been performed with the program HATTIE [99]. The design matrix for this purpose was created with the CRYSTALS software [100].

Table 17: Measurement details

Molecular formula	$[C_{36}H_{75}Fe_7N_6O_{18}](ClO_4)_2$
Formula weight	365.09 g*mol^{-1}
Temperature	100(2) K
Wavelength	0.71073 Å (MoKα)
Crystal system, space group	Cubic, $Pa\bar{3}$ (205)
a, b, c	22.0884(6) Å
Volume	10776.9(8) Å^3
Z, Calculated density	8, 1.812 g/cm^3
Absorption coefficient	2.020 mm^{-1}
F(000)	6056
Crystal size	$80 \times 90 \times 220$ μm^3
$(\frac{\sin\theta}{\lambda})_{max}$	0.42 Å^{-1}
Limiting indices	-35 $\leq h \leq$ 30
	-34 $\leq k \leq$ 35
	-33 $\leq l \leq$ 31
Refl. collected / unique / observed	211368 / 7962 / 6121 [R$_{int}$ = 0.0470]
Completeness to $\theta = 35.047°$	100%
Number of parameters	236
Number of restraints	0
R1/wR2 [$I > 2\sigma(I)$]	0.0279 / 0.0629
R1/wR2 [all refl.]	0.0470 / 0.0695
Goodness of Fit	1.022
Residual density [min/max]	-0.466 / 0.667 eÅ^{-3}

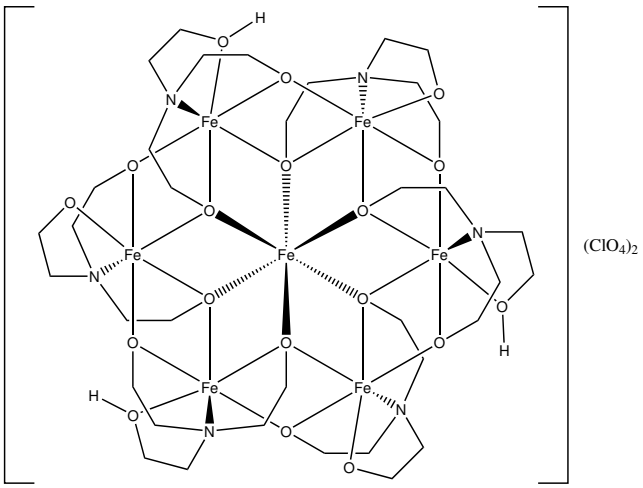

Scheme 11: Molecular structure of the title compound.

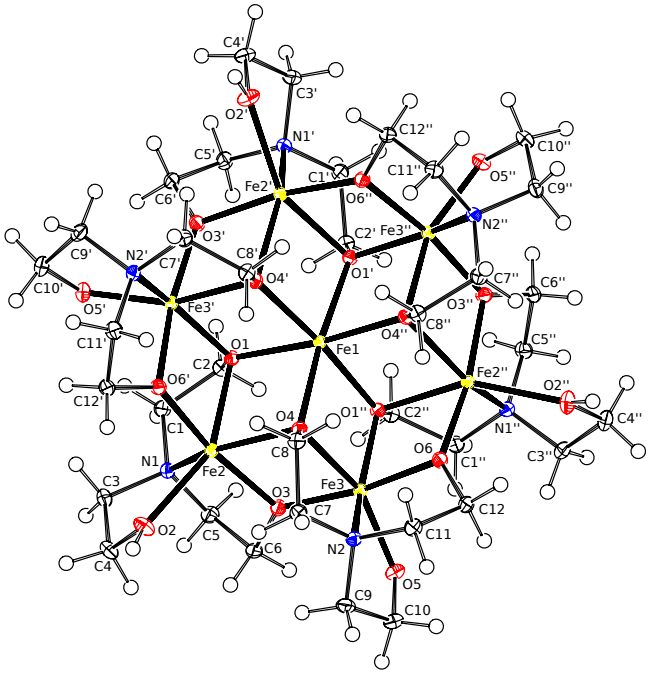

Figure 31: Displacement ellipsoid plot of the cation drawn at 50% probability. Hydrogen atoms are drawn at arbitrary radii. Perchlorate anions are omitted for clarity. Symmetry codes i: y,z,x; ii: z,x,y.

6.5 Structure determination in space group $Ia\bar{3}$

Re-refinement of the literature structure with our newly collected reflection data in space group $I2_13$ results in low R-values of $R1[I > 2\sigma(I)] = 0.0252$ and $wR2$[all refl.] = 0.0633. The Flack parameter [101] was included in the refinement as 2-component inversion twin and resulted in a value of $x = 0.51(5)$. A major problem in the refinement are very large correlation matrix elements with magnitudes upto 0.964 leading to an instable refinement. Such instable situations are known from the literature for structures where the inversion centre has accidentially been omitted. [102] As a consequence we have to consider the $Fe - O$ distances as unreliable in this space group.

As suggested by the PLATON software (see above), we transformed the $I2_13$ structure into the centrosymmetric supergroup $Ia\bar{3}$. As expected, this immediately solved the problem of large correlations. There are no correlation matrix elements larger than 0.5, here. In the $Ia\bar{3}$ supergroup Fe1 is on a special position with $\bar{3}$ symmetry (Wyckoff position b) and Fe2 on a general position. The R-values are now $R1[I > 2\sigma(I)] = 0.0239$ and $wR2$[all refl.] = 0.0606.

In $Ia\bar{3}$ we have to be concerned about only one symmtery independent short $O - O$ distance. It is here the $O2 - O2^i$ distance of 2.6144(15) Å (symmetry code i: 1-x 1/2-y z). With the reflection data available, we are now able to investigate the residual density between these two atoms (Figure 32). There is indeed a strong indication for the presence of a hydrogen atom close to the twofold axis, the midpoint between $O2$ and $O2^i$. This can be interpreted as double well situation. [53] The hydrogen atom can only be half occupied resulting

in a molecular formula of $C_{36}H_{75}Fe_7N_6O_{18}$ for the cation. Of course, the larger number of hydrogen atoms will have consequences for the iron oxidation states. $Fe-O$ distances of 2.1514(8) Å for Fe1 and 1.9667(8) to 2.1654(8) Å for Fe2 do not allow a clear distinction of oxidation state between the two indpendent iron atoms. It should also be noted that the $Fe2-O2$ bond fails with 0.0282 Å^2 and $Fe2-O1^{ii}$ with 0.0185 Å^2 to the Hirshfeld rigid bond test [103] as implemented in PLATON [44] (symmetry code ii: 1/2-y,1/2-z,1/2-x). Failure to the rigid bond test due to elongated displacement ellipsoids has been reported for average structures of Jahn-Teller distorted complexes (see for example [104] and [105]). In the present structure it can indicate an average structure as well. The physically unreasonable displacement behaviour can clearly be seen in a PEANUT plot (Figure 36, left).

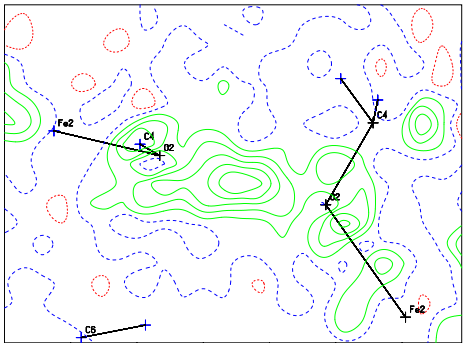

Figure 32: Residual density calculation around atom $O2$ in space group $Ia\bar{3}$. Contour levels are drawn at -0.20 (red), 0.10 (blue) and 0.60 (green) eÅ^{-3}. Calculations were done with PLATON. [44]

6.6 Structure determination in space group $Pa\bar{3}$

A closer inspection of the diffraction pattern shows that reflections with $h+k+l = 2n$ are weak but not absent. Space group $Ia\bar{3}$ represents thus an average structure and the true space group is subgroup $Pa\bar{3}$ with a volume of the unit cell 10776.9(8) Å^3. After re-integration of the data based on the new cell, least-squares refinement in $Pa\bar{3}$ is stable. The largest element of the correlation matrix is 0.521, just above the 0.5 cutoff. As in subgroup $I2_13$, Fe1 is on a threefold axis here and Fe2 and Fe3 are on general positions (Figure 31). The main difference is that subgroup $I2_13$ is obtained by the removal of an inversion centre while the true space group $Pa\bar{3}$ is obtained by the removal of translational symmetry. Consequences for the intramolecular geometry are minor but significant (see below). A major difference concerns the short intermolecular $O-O$ contact. In $I2_13$ this involves symmetry related atom pairs $O2/O2^i$ and $O5/O5^{ii}$ (symmetry code i: -x 1/2-y z; ii: 1/2-x y 2-z), while in $Pa\bar{3}$ the two oxygen atoms of the potential hydrogen bond are symmetry independent (Figure 35). There is no symmetry element between the potential donor and acceptor oxygen atoms.

Figure 34 shows the residual electron density between $O2$ and $O5^{iii}$ (symmetry code iii: z 1/2-x 1/2+y). The hydrogen atom is clearly bound to $O2$ and can be introduced with full occupancy. $O5^{iii}$ is then the acceptor of the hydrogen bond (table hydrogen bond). From the nearly linear geometry and rather short

$O\cdots O$ distance we conclude that the hydrogen bond is very strong. Overall, the hydrogen bonding leads to a three-dimensional network in the crystal. The different protonation state for $O2$ and $O5$ is also reflected in the $Fe-O$ distances. $Fe2-O2$ of 2.2081(9) Å is significantly longer than $Fe3-O5$ with 1.9600(8) Å. This difference can be used for the bond-valence calculations (see below). All $Fe-O$ bonds now have reasonably low values for the Hirshfeld rigid bond test with a maximum of 0.0024 Å^2. Also, the PEANUT plot looks physically reasonable (Figure 36, right). The R-value of the rigid-body model improves from 0.238 ($Ia\bar{3}$) to 0.160 ($Pa\bar{3}$) ($R = \{\sum[(U_{obs}-U_{calc})^2]/\sum(U_{obs})^2\}^{1/2}$) [106].

The IR data given in the publication of Liu et al. [71] shows a broad peak at 3463 cm^{-1}. This can be an indication for the presence of an O-H group. We repeated the IR experiment on our crystals and indeed found a very broad peak in the same region.

The differences between the average structure in $Ia\bar{3}$ and the true structure in $Pa\bar{3}$ are mainly expressed in the weak superstructure reflections with $h+k+l = 2n+1$. Reflection statistics are given in Table 19. $\langle I/\sigma\rangle$ of the substructure reflections are 3.2 fold stronger than the superstructure reflections. Still, 69.44% of the superstructure reflections are stronger than the 2σ criterion. The pseudo-translation symmetry can also be seen in the Patterson map calculated with SHELXS97 [107]. The highest non-origin peak is at $(\frac{1}{2},\frac{1}{2},\frac{1}{2})$ with a height of 346 compared to the normalized height of 999 at the origin. Within the default tolerances PLATON ADDSYM gives a 100% fit for I-centered superstructure ($Ia\bar{3}$). The maximum deviation is 0.35 Å and involves the $O2/O5$ atom pair. The cation has an exact, crystallographic C_3 symmetry and an approximate C_{3i} symmetry with an r.m.s. deviation of 0.0750 for the non-hydrogen atoms. [49] The C_{3i} symmetry is mainly broken by the O-H hydrogen atoms (Figure 33).

A leverage analysis [99] gives a quantitative insight on the influence of observations on the refined parameters. We were especially interested in which reflections have the largest influence on the position of hydrogen atom $H2$. The largest T^2 values for the x, y and z coordinates are given in Table 20. In the current setting of the coordinates, the most influencial reflections for the x and z coordinates all belong to the weak superstructure reflections with $h+k+l = 2n+1$. The y coordinate does not have this dependency. Indeed, the $O2-O5^{iii}$ direction of the hydrogen bond is nearly perpendicular to the b-axis with an angle of 90.46(4)°.

Table 18: Geometry of the hydrogen bond in space group $Pa\bar{3}$ (symmetry code iii: z 1/2-x 1/2+y).

	$D-H$	$H-A$	$D-A$	$D-H-A$
$O2-H2\cdots O5^{iii}$	0.89(2) Å	1.73(2) Å	2.6137(13) Å	176(2)°

Table 19: Reflection statistics for the strong substructure and the weak superstructure reflections. Agreement factors R1 and wR2 were calculated according to the SHELXL manual. [21]

$h+k+l$	#	$\langle I \rangle$	$\langle \sigma \rangle$	$\langle I \rangle / \langle \sigma \rangle$	$\langle I/\sigma \rangle$	wR2(all)	R1($I > 2\sigma$)	$I \geq 2\sigma$
2n	3990	12721.86	495.31	25.68	46.01	0.0621	0.0233	84.29%
2n+1	3972	1654.41	131.84	12.55	15.64	0.0894	0.0412	69.44%
total	7962	7198.77	313.97	22.93	30.85	0.0701	0.0282	76.88%

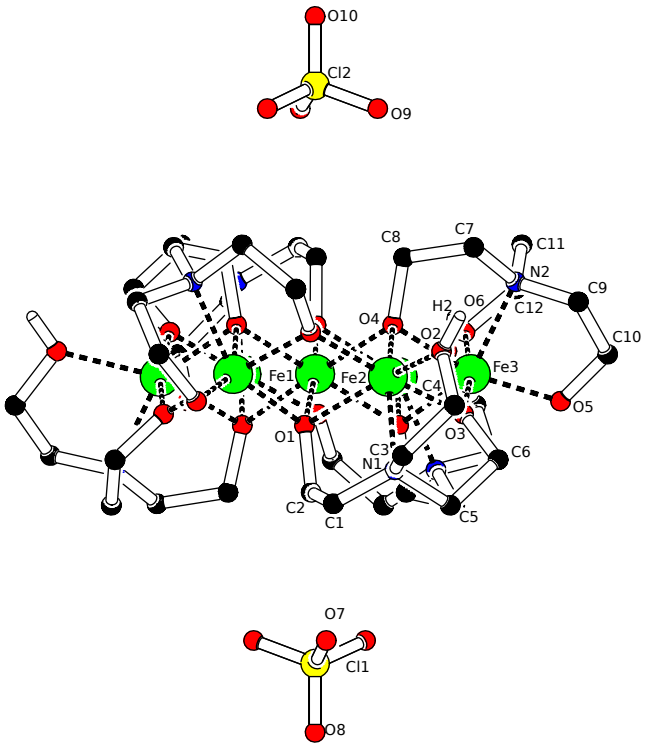

Figure 33: Side view of the title compound. The approximate inversion symmetry is mainly violated by the O-H hydrogen atoms. C-H hydrogen atoms are omitted for clarity.

Table 20: Results of the leverage analysis performed with the program HATTIE [99]. The normalized value T^2 is a measure of the influence of a specific reflection on a refined parameter.

	h	k	l	T^2
x coordinate (H2)	3	1	5	10000
	3	3	3	7629.49
	3	5	7	7353.62
	5	1	7	7175.33
y coordinate (H2)	0	2	6	10000
	0	6	10	7304.21
	5	1	8	5936.25
	6	4	10	5243.41
z coordinate (H2)	5	0	6	10000
	4	6	7	5790.49
	1	0	8	5227.58
	3	4	6	4357.97

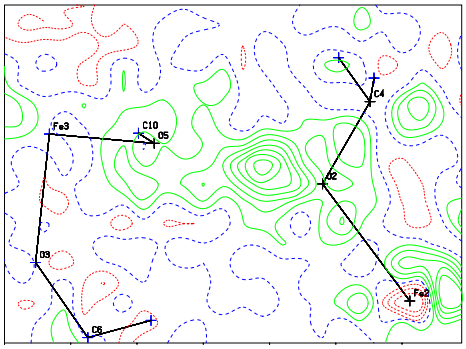

Figure 34: Residual density calculation in space group $Pa\bar{3}$. The peak centered at 0.915 Å from $O2$ shows that the discussed hydrogen atom $H2$ is likely connected to $O2$. Contour levels are drawn at -0.40 (red), 0.10 (blue) and 0.70 (green) $e\text{Å}^{-3}$. Calculations were done with PLATON. [44]

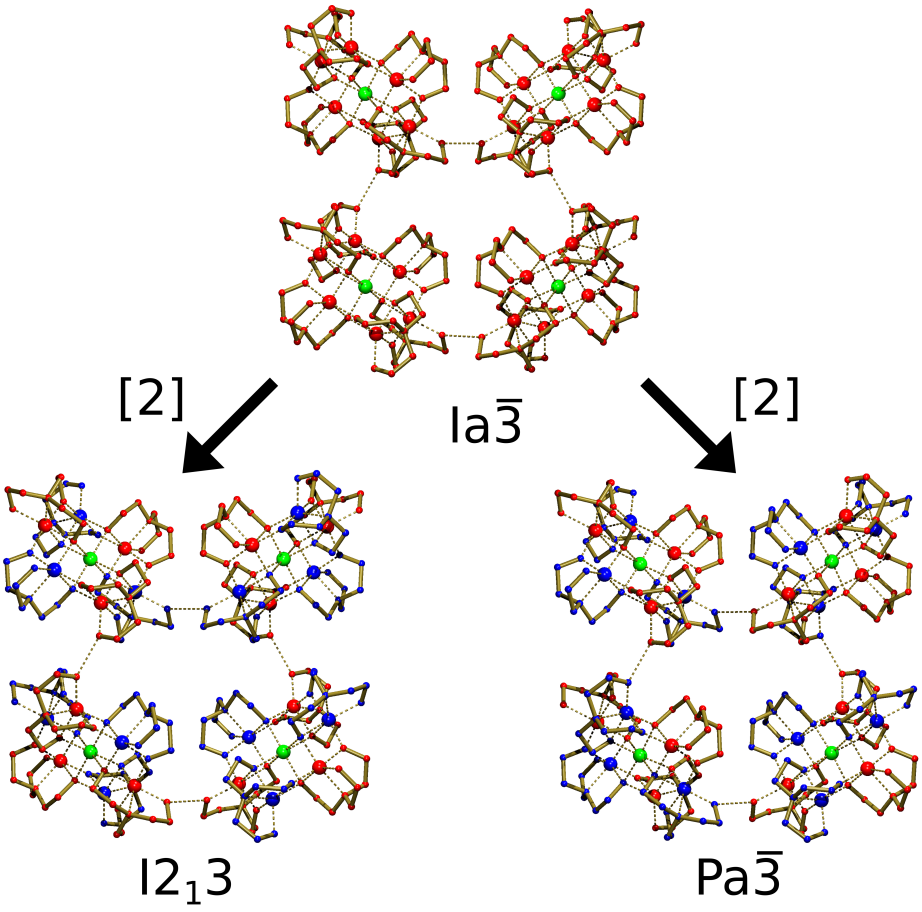

Figure 35: Coordination between adjacent cations in each of the described space groups. Dashed lined between the cations represent short (< 2.7Å) $O-O$ distances. Each color represents a crystallographically independent part of the complex. The supergroup $Ia\bar{3}$ can be transformed into one of the subgroups $I2_13$ and $Pa\bar{3}$, both with subgroup index 2.

6.7 Bond valence analysis

As discussed above, the space group choice results in different symmetries of the Fe sites. A summary of the corresponding $Fe-O$ distances is given in Table 21. We assume that the distances in $I2_13$ are unreliable because of an unstable least-squares refinement. The distances in $Ia\bar{3}$ reflect the situation of an average structure. In the true space group $Pa\bar{3}$ there are three symmetry independent iron sites. The $Fe-O$ distances for Fe3 (general position) are shorter than the distances for Fe1 (special position, threefold axis) and Fe2 (general position).

Based on the difference of bond distances, I.D. Brown introduced the concept of bond-valence analysis for the determination of oxidation states. [52] An overview is shown in Table 22. The published values for the bond-valence sum (BVS) in the literature structure are rather inconclusive. [71] With the correct space group choice $Pa\bar{3}$, we can conclude that Fe1 and Fe2 are in oxidation state

+2, while Fe3 is in oxidation state +3. This is conclusive with the addition of O-H hydrogen atoms which were missing in the literature structure.

Table 21: Bond lengths [Å] from different refinements.

	Literature at RT [71]	Present study at 110 K		
	$I2_13$	$I2_13$	$Ia\bar{3}$	$Pa\bar{3}$
$Fe1-O$	2.123(6) - 2.181(5)	2.140(4) - 2.163(5)	2.1514(8)	2.1352(8) - 1.1719(8)
$Fe2-O$	1.977(6) - 2.183(6)	1.976(4) - 2.166(5)	1.9667(8) - 2.1654(8)	1.9814(8) - 2.2342(8)
$Fe3-O$	1.953(6) - 2.151(6)	1.956(5) - 2.165(5)	-	1.9516(8) - 2.0989(8)

Table 22: Bond-valence sums (BVS). Entries for the literature structure were taken from the original publication. Entries for the present study were calculated using the ToposPro software [67].

	Assumed state	Literature at RT [71]	Present study at 110 K		
		$I2_13$	$I2_13$	$Ia\bar{3}$	$Pa\bar{3}$
Fe1	+2	1.82	1.94	1.94	1.93
	+3		2.08	2.08	2.07
Fe2	+2		2.50	2.50	2.21
	+3	2.53	2.65	2.65	2.34
Fe3	+2		2.50		2.85
	+3	2.73	2.65		3.02

6.8 Rigid-body analysis

A rigid-body analysis with the programs THMA11 [106] and PEANUT [108] shows how the atomic displacements in the structure deviate from rigid-body behaviour. From the PEANUT plots (Figure 36) it is clear that the atomic displacement in $Ia\bar{3}$ is quite incoherent as compared to $Pa\bar{3}$. This indicates that the structure in $Ia\bar{3}$ is still inaccurate, especially considering atoms $O2$ and $O3$, which show very large displacement differences.

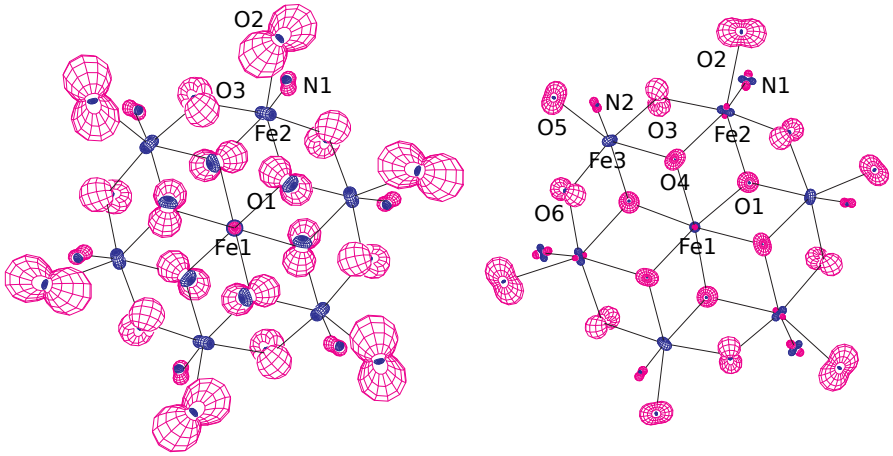

Figure 36: Peanut plots [108] showing the difference between the measured displacement parameters and the parameters obtained by rigid-body analyses using the program THMA11 [106] A scale factor of 6.15 was used for the r.m.s. surfaces. Red surfaces indicate positive differences and blue surfaces negative differences. Left: space group $Ia\bar{3}$; right: space group $Pa\bar{3}$

6.9 Conclusions

The current study was initiated because the PLATON validation software [44] hints on severe problems with the literature structure [71]. In the course of our investigations it appeared that weak superstructure reflections were essential for the determination of the Fe-oxidation states as well as of the hydrogen bonding situation. The original publication did not include reflection data. Even if they were available, it would be impossible to detect the missing translation symmetry and the original problem with reflection indexing. This can only be detected if the original diffraction images are available. Fortunately, there are initiatives trying to set up an archiving system for diffraction images [109].

7 Final conclusions and outlook

The crystal structures of salicylic acid, Mn(II) salicylate dihydrate and Zn(II) salicylate dihydrate were solved by X-ray crystallography and subjected to a toplogical analysis. Our crystal structure of salicylic acid, which had previously been reported by Munshi and Guru Row [17], showed a significant improvement in data quality as compared to the literature data. The topological analysis shows that the C(1)-C(2) bond, which is broken during the oxidation reaction in SDO, also happens to be the longest and weakest aromatic bond. A comparison of the aromatic bonds in salicylic acid and to the equivalent bonds in the metal-coordinated salicylate ligands shows a discrepancy in the bond length of the C(1)-C(2) bond. This could however not be directly attributed to metal-coordination effects, as the C(1)-C(2) bond length difference between both of the Mn-coordinated salicylate ligands is similar to the bond length difference between free salicylic acid and the metal-coordinated salicylates.

Additionally, two novel Fe(III) salicylate complexes were synthesized and

crystallized: iron(III) salicylate dihydrate and triethanolaminato iron(III) salicylate. Both crystal structures were of insufficient quality for a topological analysis and were therefore not included in the bond length comparison.

The crystal structure of iron(III) salicylate dihydrate is the first reported crystal structure of Fe(III) salicylate without additional counterions. The oxidation state +3 of iron is balanced by two salicylate ligands which are deprotonated at the hydroxyl group and share a single carboxylate hydrogen atom with their symmetry equivalent. This crystal provided an interesting case of reticular twinning.

Triethanolaminato iron(III) salicylate was synthesized in an attempt to create a more accurate analogue for the catalytic site of SDO. The synthesized complex was however not directly analogous to the catalytic site SDO. Instead, the obtained crystal structure revealed anionic complexes with 4 iron atoms in which the iron centres are coordinated by either triethylamine or salicylate. Also in this complex, all iron atoms were found to be in oxidation state +3.

During a literature search for multi-centre iron complexes in the context of the previous experiment, the crystal structure of triethylaminato iron was found. [71] Short O-O distances and obviously missed symmetry prompted us to resynthesize the complex and re-evaluate its crystal structure. A change of space group was found, as well as additional hydrogen atoms which were missing in the original structure. The iron oxidation states were found to be $Fe_4^{II}Fe_3^{III}$ instead of $Fe^{II}Fe_6^{III}$.

The current study has not resulted in a full understanding of the catalytic site in SDO. Nevertheless, we made progress in understanding the complex-forming behaviour of salicylic acid. The acquired knowledge may be used for designing follow-up experiments. The complexes described in the present study contain valuable information on metal-binding effects on salicylic acid. Higher quality X-ray diffraction data (and therefore better crystals) are needed to acquire this information. This can be approached by further optimizing the experimental conditions. For instance, the synthesis procedure for iron(III) salicylate dihydrate could be optimized by varying the concentrations of the reagents. Crystal growth of triethanolaminato iron(III) salicylate can be improved by finding a more effective solvent-antisolvent pair or applying an entirely different crystallization technique such as gel crystallization.

In future experiments, it may be worthwhile to synthesize iron salicylate complexes with a variety of tridentate and tetradentate ligands to simulate the catalytic site in SDO. Especially ligands which coordinate via nitrogen atoms, representing histidine residues, may lead to a more accurate biomimetic complex for this enzyme.

Although salts of Fe^{2+} were used as a reagent for all iron-salicylate complexes, attempts to crystallize iron(II) salicylate complexes were not successful yet. They are extremely sensitive and easily oxidized to Fe(III). For synthesis of iron(II) salicylate, it is critical to work in an oxygen and water free environment. Because of the very fast complexation behaviour of iron(III) salicylate [35], it is recommended to use a slow simultaneous complexation-crystallization method such as gel crystallization for iron(II) salicylate as well.

References

[1] P. C. A. Bruijnincx, M. Lutz, A. L. Spek, W. R. Hagen, B. M. Weckhuysen, G. van Koten, and R. J. M. K. Gebbink, "Modeling the 2-his-1-carboxylate facial triad: Ironcatecholato complexes as structural and functional models of the extradiol cleaving dioxygenases," *Journal of the American Chemical Society*, vol. 129, no. 8, pp. 2275–2286, 2007. PMID: 17266307.

[2] D. Buongiorno and G. D. Straganz, "Structure and function of atypically coordinated enzymatic mononuclear non-heme-Fe(II) centers," *Coordination Chemistry Reviews*, vol. 257, pp. 541–563, Jan 2013.

[3] M. Costas, M. P. Mehn, M. P. Jensen, and L. Que, "Dioxygen activation at mononuclear nonheme iron active sites: Enzymes, models, and intermediates," *Chem. Rev.*, vol. 104, pp. 939–986, Feb 2004.

[4] M. Ferraroni, I. Matera, L. Steimer, S. Bürger, A. Scozzafava, A. Stolz, and F. Briganti, "Crystal structures of salicylate 1,2-dioxygenase-substrates adducts: A step towards the comprehension of the structural basis for substrate selection in class III ring cleaving dioxygenases," *Journal of Structural Biology*, vol. 177, pp. 431–438, Feb 2012.

[5] B. Meunier, *Biomimetic Oxidations Catalyzed by Transition Metal Complexes*. Imperial College Pr., 2000.

[6] J. S. Pap, A. Matuz, G. Baráth, B. Kripli, M. Giorgi, G. Speier, and J. Kaizer, "Bio-inspired flavonol and quinolone dioxygenation by a nonheme iron catalyst modeling the action of flavonol and 3-hydroxy-4(1H)-quinolone 2,4-dioxygenases," *Journal of Inorganic Biochemistry*, vol. 108, pp. 15–21, Mar 2012.

[7] R. Rahaman, B. Chakraborty, and T. K. Paine, "Mimicking the aromatic-ring-cleavage activity of gentisate-1,2-dioxygenase by a nonheme iron complex," *Angewandte Chemie*, vol. 128, pp. 14042–14046, Sep 2016.

[8] S. Taktak, M. Flook, B. M. Foxman, L. Que, Jr., and E. V. Rybak-Akimova, "ortho-hydroxylation of benzoic acids with hydrogen peroxide at a non-heme iron center," *Chemical Communications*, pp. 5301–5303, Aug 2005.

[9] T. Borowski and P. E. M. Siegbahn, "Mechanism for catechol ring cleavage by non-heme iron intradiol dioxygenases: A hybrid DFT study," *Journal of the American Chemical Society*, vol. 128, pp. 12941–12953, Oct 2006.

[10] G. J. Christian, S. Ye, and F. Neese, "Oxygen activation in extradiol catecholate dioxygenases - a density functional study," *Chemical Science*, vol. 3, no. 5, p. 1600, 2012.

[11] G. Dong, S. Shaik, and W. Lai, "Oxygen activation by homoprotocatechuate 2,3-dioxygenase: a QM/MM study reveals the key intermediates in the activation cycle," *Chemical Science*, vol. 4, no. 9, p. 3624, 2013.

[12] W. Lewandowski, M. Kalinowska, and H. Lewandowska, "The influence of metals on the electronic system of biologically important ligands. spectroscopic study of benzoates, salicylates, nicotinates and isoorotates. review," *Journal of Inorganic Biochemistry*, vol. 99, pp. 1407–1423, Jul 2005.

[13] I. Matera, M. Ferraroni, S. Brger, A. Scozzafava, A. Stolz, and F. Briganti, "Salicylate 1,2-dioxygenase from Pseudaminobacter Salicylatoxidans: Crystal structure of a peculiar ring-cleaving dioxygenase," *Journal of Molecular Biology*, vol. 380, p. 856868, Jul 2008.

[14] M. A. Miller and J. D. Lipscomb, "Homoprotocatechuate 2,3-dioxygenase from Brevibacterium Fuscum: A dioxygenase with catalase activity," *Journal of Biological Chemistry*, vol. 271, p. 55245535, Mar 1996.

[15] S. Roy and J. Kästner, "Synergistic substrate and oxygen activation in salicylate dioxygenase revealed by QM/MM simulations," *Angewandte Chemie International Edition*, vol. 55, pp. 1168–1172, Nov 2015.

[16] R. F. W. Bader, "Atoms in molecules," *Accounts of Chemical Research*, vol. 18, no. 1, pp. 9–15, 1985.

[17] P. Munshi and T. N. Guru Row, "Intra- and intermolecular interactions in small bioactive molecules: cooperative features from experimental and theoretical charge-density analysis," *Acta Crystallographica Section B Structural Science*, vol. 62, p. 612626, Jul 2006.

[18] A. M. M. Schreurs, X. Xian, and L. M. J. Kroon-Batenburg, "*EVAL15*: a diffraction data integration method based on *ab initio* predicted profiles," *Journal of Applied Crystallography*, vol. 43, pp. 70–82, Feb 2010.

[19] G. M. Sheldrick, "Sadabs," *Universität Göttingen, Germany*, 2008.

[20] G. M. Sheldrick, "*SHELXT* – Integrated space-group and crystal-structure determination," *Acta Crystallographica Section A*, vol. 71, pp. 3–8, Jan 2015.

[21] G. M. Sheldrick, "Crystal structure refinement with *SHELXL*," *Acta Crystallographica Section C*, vol. 71, pp. 3–8, Jan 2015.

[22] A. Volkov, P. Macchi, L. Farrugia, C. Gatti, P. Mallinson, T. Richter, and T. Koritsanszky, "XD2016–a computer program package for multipole refinement, topological analysis of charge densities and evaluation of intermolecular energies from experimental and theoretical structure factors," *Program Version*, vol. 5, 2016.

[23] R. F. Stewart, E. R. Davidson, and W. T. Simpson, "Coherent X-ray scattering for the hydrogen atom in the hydrogen molecule," *The Journal of Chemical Physics*, vol. 42, no. 9, pp. 3175–3187, 1965.

[24] R. F. Stewart, J. Bentley, and B. Goodman, "Generalized X-ray scattering factors in diatomic molecules," *The Journal of Chemical Physics*, vol. 63, no. 9, pp. 3786–3793, 1975.

[25] N. K. Hansen and P. Coppens, "Testing aspherical atom refinements on small-molecule data sets," *Acta Crystallographica Section A*, vol. 34, pp. 909–921, Nov 1978.

[26] E. Clementi and C. Roetti, "Roothaan-Hartree-Fock atomic wavefunctions: Basis functions and their coefficients for ground and certain excited states of neutral and ionized atoms, z54," *Atomic Data and Nuclear Data Tables*, vol. 14, no. 34, pp. 177 – 478, 1974.

[27] K. Meindl and J. Henn, "Foundations of residual-density analysis," *Acta Crystallographica Section A Foundations of Crystallography*, vol. 64, pp. 404–418, apr 2008.

[28] A. Ø. Madsen, "*SHADE* web server for estimation of hydrogen anisotropic displacement parameters," *Journal of Applied Crystallography*, vol. 39, pp. 757–758, Oct 2006.

[29] A. R. Campanelli, A. Domenicano, and F. Ramondo, "Electronegativity, resonance, and steric effects and the structure of monosubstituted benzene rings: an ab initio MO study," *The Journal of Physical Chemistry A*, vol. 107, no. 33, pp. 6429–6440, 2003.

[30] K. Rissanen, J. Valkonen, P. Kokkonen, M. Leskel, and L. Niinist, "Structural and thermal studies on salicylato complexes of divalent manganese, nickel, copper and zinc.," *Acta Chemica Scandinavica*, vol. 41a, p. 299309, 1987.

[31] S. K. Langley, N. F. Chilton, B. Moubaraki, and K. S. Murray, "Self-assembled decanuclear $Na^{I}{}_{2}Mn^{II}{}_{4}Mn^{III}{}_{4}$ complexes: from discrete clusters to 1-D and 2-D structures, with the $Mn^{II}{}_{4}Mn^{III}{}_{4}$ unit displaying a large spin ground state and probable smm behaviour," *Dalton Transactions*, vol. 40, no. 45, pp. 12201–12209, 2011.

[32] H. Arend and J. Connelly, "Tetramethoxysilane as gel forming agent in crystal growth," *Journal of Crystal Growth*, vol. 56, no. 3, pp. 642–644, 1982.

[33] J. A. van der Horn, B. Souvignier, and M. Lutz, "Crystallization, Structure Determination and Reticular Twinning in Iron(III) Salicylate: $Fe[(HSal)(Sal)(H_2O)_2]$," *Crystals*, vol. 7, art. 377, 2017.

[34] R. C. Hider and T. Zhou, "The design of orally active iron chelators," *Annals of the New York Academy of Sciences*, vol. 1054, no. 1, pp. 141–154, 2005.

[35] K. R. Reid, M. E. Meyerhoff, and J. T. Mitchell-Koch, "Salicylate detection by complexation with iron(III) and optical absorbance spectroscopy. an undergraduate quantitative analysis experiment," *Journal of Chemical Education*, vol. 85, pp. 1658–1659, Dec 2008.

[36] I. P. Pozdnyakov, V. F. Plyusnin, V. P. Grivin, and E. Oliveros, "Photochemistry of Fe(III) complexes with salicylic acid derivatives in aqueous solutions," *Journal of Photochemistry and Photobiology A: Chemistry*, vol. 307 - 308, pp. 9 – 15, 2015.

[37] W. A. E. McBryde, J. L. Rohr, J. S. Penciner, and J. A. Page, "Stability constants of three iron(III) salicylates," *Canadian Journal of Chemistry*, vol. 48, p. 25742586, Aug 1970.

[38] M. V. Park, "Complex formation between iron(III) and some substituted salicylic acids," *J. Chem. Soc. A*, pp. 816–820, 1966.

[39] M. Chattopadhyaya, "Effect of substituents on the relative stabilities of Fe(III) complexes of substituted salicylic acids," *Journal of the Indian Chemical Society*, vol. 59, no. 11-1, pp. 1416–1418, 1982.

[40] E. Furia and G. Sindona, "Interaction of iron(III) with 2-Hydroxybenzoic acid in aqueous solutions," *Journal of Chemical & Engineering Data*, vol. 57, p. 195199, Jan 2012.

[41] S. K. Porwal, E. Furia, M. E. Harris, R. Viswanathan, and L. Devireddy, "Synthetic, potentiometric and spectroscopic studies of chelation between Fe(III) and 2,5-DHBA supports salicylate-mode of siderophore binding interactions," *Journal of Inorganic Biochemistry*, vol. 145, no. Supplement C, pp. 1 – 10, 2015.

[42] A. J. M. Duisenberg, "Indexing in single-crystal diffractometry with an obstinate list of reflections," *Journal of Applied Crystallography*, vol. 25, pp. 92–96, Apr 1992.

[43] G. M. Sheldrick, "Experimental phasing with *SHELXC/D/E*: combining chain tracing with density modification," *Acta Crystallographica Section D*, vol. 66, pp. 479–485, Apr 2010.

[44] A. L. Spek, "Structure validation in chemical crystallography," *Acta Crystallographica Section D*, vol. 65, pp. 148–155, Feb 2009.

[45] G. Sheldrick, "Twinabs, version 2012/1," *University of Göttingen, Germany*, 2012.

[46] R. Herbst-Irmer and G. M. Sheldrick, "Refinement of Twinned Structures with *SHELXL*97," *Acta Crystallographica Section B*, vol. 54, pp. 443–449, Aug 1998.

[47] A. Thorn, B. Dittrich, and G. M. Sheldrick, "Enhanced rigid-bond restraints," *Acta Crystallographica Section A: Foundations of Crystallography*, vol. 68, no. 4, pp. 448–451, 2012.

[48] K. Robinson, G. V. Gibbs, and P. H. Ribbe, "Quadratic elongation: A quantitative measure of distortion in coordination polyhedra," *Science*, vol. 172, no. 3983, pp. 567–570, 1971.

[49] T. Pilati and A. Forni, "*SYMMOL*: a program to find the maximum symmetry group in an atom cluster, given a prefixed tolerance," *Journal of Applied Crystallography*, vol. 31, pp. 503–504, Jun 1998.

[50] V. M. Nurchi, M. Crespo-Alonso, L. Toso, J. I. Lachowicz, G. Crisponi, G. Alberti, R. Biesuz, A. Domínguez-Martín, J. Niclós-Gutíerrez, J. M. González-Pérez, and M. A. Zoroddu, "Iron(III) and aluminium(III) complexes with substituted salicyl-aldehydes and salicylic acids," *Journal of Inorganic Biochemistry*, vol. 128, pp. 174–182, nov 2013.

[51] J. Zarembowitch, O. Kahn, J. Jaud, and J. Galy, "Versatility of iron(III) upon coordination with the binucleating ligand N, N'-bis-(2-hydroxy, 3-carboxybenzilidene) 1, 2-diaminoethane," *Inorganica Chimica Acta*, vol. 65, pp. L35–L36, 1982.

[52] I. D. Brown, *The Chemical Bond in Inorganic Chemistry.* Oxford University Press, 2016.

[53] P. Gilli, V. Bertolasi, L. Pretto, V. Ferretti, and G. Gilli, "Covalent versus electrostatic nature of the strong hydrogen bond: discrimination among single, double, and asymmetric single-well hydrogen bonds by variable-temperature X-ray crystallographic methods in β-diketone enol RAHB systems," *Journal of the American Chemical Society*, vol. 126, pp. 3845–3855, mar 2004.

[54] X.-Z. Li, B. Walker, and A. Michaelides, "Quantum nature of the hydrogen bond," *Proceedings of the National Academy of Sciences*, vol. 108, no. 16, pp. 6369–6373, 2011.

[55] A. Farajtabar and F. Gharib, "Solvent effect on protonation constants of salicylic acid in mixed aqueous organic solutions of DMSO," *Monatshefte für Chemie-Chemical Monthly*, vol. 141, no. 4, pp. 381–386, 2010.

[56] M. García, G. Ramis, and C. Mongay, "Spectrophotometric determination of protonation constants of monoprotic systems in strong acid and strong basic media," *Spectrochimica Acta Part A: Molecular Spectroscopy*, vol. 38, no. 9, pp. 1005–1009, 1982.

[57] Z. Ma, W. Lu, B. Liang, and A. J. L. Pombeiro, "Synthesis, characterization, photoluminescent and thermal properties of zinc(II) 4'-phenyl-terpyridine compounds," *New J. Chem.*, vol. 37, pp. 1529–1537, 2013.

[58] P. Seth, S. Ghosh, A. Figuerola, and A. Ghosh, "Trinuclear heterometallic Cu^{II}-Mn^{II} complexes of a salen type Schiff base ligand: anion dependent variation of phenoxido bridging angles and magnetic coupling," *Dalton Trans.*, vol. 43, pp. 990–998, 2014.

[59] N. Palanisami, P. Rajakannu, and R. Murugavel, "Non-covalently aggregated zinc and cadmium complexes derived from substituted aromatic carboxylic acids: Synthesis, spectroscopy, and structural studies," *Inorganica Chimica Acta*, vol. 405, pp. 522 – 531, 2013.

[60] T. Terada, K. Hirabayashi, D. Liu, T. Nakamura, T. Wakimoto, T. Matsumoto, and K. Tatsumi, "[3:1] site-differentiated [4Fe-4S] clusters having one carboxylate and three thiolates," *Inorganic Chemistry*, vol. 52, no. 20, pp. 11997–12004, 2013. PMID: 24102391.

[61] C. R. Groom and F. H. Allen, "The Cambridge Structural Database in retrospect and prospect," *Angewandte Chemie International Edition*, vol. 53, no. 3, pp. 662–671, 2014.

[62] P. Lemoine, A. Tomas, D. Nguyen-Huy, and B. Viossat, "Crystal structure of aquachloro (salicylato)(1,10-phenanthroline)-copper(II), $C_{19}H_{15}ClCuN_2O_4$," *Zeitschrift für Kristallographie-New Crystal Structures*, vol. 215, no. 4, pp. 521–522, 2000.

[63] C. Banti, A. Giannoulis, N. Kourkoumelis, A. Owczarzak, M. Kubicki, and S. Hadjikakou, "Silver(I) compounds of the anti-inflammatory agents salicylic acid and p-hydroxyl-benzoic acid which modulate cell function," *Journal of inorganic biochemistry*, vol. 142, pp. 132–144, 2015.

[64] C. F. Edwards, W. P. Griffith, A. J. White, and D. J. Williams, "A new bonding mode for salicylate: The X-ray crystal structure of (pyH)[MoO_2(Hsal)(sal)]," *Polyhedron*, vol. 11, no. 20, pp. 2711–2712, 1992.

[65] N. Palanisami, G. Prabusankar, and R. Murugavel, "A novel dimeric copper salicylate with an undissociated COOH group: Synthesis and crystal structure of [Cu_2(HSal)(Sal)(2,2-bpy)2](ClO_4)," *Inorganic Chemistry Communications*, vol. 9, no. 10, pp. 1002–1006, 2006.

[66] T. E. Baroni, S. Bembenek, J. A. Heppert, R. R. Hodel, B. B. Laird, M. D. Morton, D. L. Barnes, and F. Takusagawa, "Hydrogen bonding in tungsten (VI) salicylate free acids," *Coordination chemistry reviews*, vol. 174, no. 1, pp. 255–282, 1998.

[67] V. A. Blatov, A. P. Shevchenko, and D. M. Proserpio, "Applied topological analysis of crystal structures with the program package ToposPro," *Crystal Growth & Design*, vol. 14, no. 7, pp. 3576–3586, 2014.

[68] R. Herbst-Irmer, *Crystal Structure Refinement: A Crystallographer's Guide to SHELXL*, ch. 7: Twinning, pp. 106–149. Oxford University Press, 2006.

[69] K. Dornberger-Schiff, "Reinterpretation of pseudo-orthorhombic diffraction patterns," *Acta Crystallographica*, vol. 21, pp. 311–322, Sep 1966.

[70] Y. Le Page, "Mallard's law recast as a diophantine system: fast and complete enumeration of possible twin laws by [reticular][pseudo] merohedry," *Journal of applied crystallography*, vol. 35, no. 2, pp. 175–181, 2002.

[71] T. Liu, B.-W. Wang, Y.-H. Chen, Z.-M. Wang, and S. Gao, "Syntheses, structures and magnetic properties of two mixed-valent disc-like hepta-nuclear compounds of $[Fe^{II}Fe^{III}_6(tea)_6](ClO_4)_2$ and $[Mn^{II}_3Mn^{III}_4(nmdea)_6(N_3)_6]\cdot CH_3OH$ (tea=$N(CH_2CH_2O)^{3-}_3$, nmdea=$CH_3N(CH_2CH_2O)^{2-}_2$)," *Zeitschrift für anorganische und allgemeine Chemie*, vol. 634, no. 4, pp. 778–783, 2008.

[72] V. Mereacre, D. Prodius, Y. Lan, C. Turta, C. E. Anson, and A. K. Powell, "Antiferromagnetically coupled iron ions in a polynuclear Fe^{III}-Dy complex: Confirmation by variable-field 57Fe Mössbauer spectroscopy," *Chemistry – A European Journal*, vol. 17, no. 1, pp. 123–128, 2011.

[73] G. Xiong, Y.-L. Hou, J.-Z. Cui, and B. Zhao, "A new octanuclear Fe8 cluster with antiferromagnetic coupling," *Inorganic Chemistry Communications*, vol. 35, pp. 89–91, 2013.

[74] A. Baniodeh, Y. Liang, C. E. Anson, N. Magnani, A. K. Powell, A.-N. Unterreiner, S. Seyfferle, M. Slota, M. Dressel, L. Bogani, *et al.*, "Unraveling the influence of lanthanide ions on intra-and inter-molecular electronic processes in $Fe_{10}Ln_{10}$ nano-toruses," *Advanced Functional Materials*, vol. 24, no. 40, pp. 6280–6290, 2014.

[75] S.-J. Liu, S.-D. Han, J.-M. Jia, L. Xue, Y. Cui, S.-M. Zhang, and Z. Chang, "Step-by-step synthesis of one Fe_6 wheel and two Fe_{10} clusters derived from a multidentate triethanolamine ligand," *CrystEngComm*, vol. 16, no. 24, pp. 5212–5215, 2014.

[76] O. Botezat, J. van Leusen, V. C. Kravtsov, A. Ellern, P. Kögerler, and S. G. Baca, "Iron(III) carboxylate/aminoalcohol coordination clusters with propeller-shaped Fe_8 cores: approaching reasonable exchange energies," *Dalton Transactions*, vol. 44, no. 47, pp. 20753–20762, 2015.

[77] S. Schmidt, D. Prodius, V. Mereacre, G. E. Kostakis, and A. K. Powell, "Unprecedented chemical transformation: crystallographic evidence for 1,1,2,2-tetrahydroxyethane captured within an Fe_6Dy_3 single molecule magnet," *Chemical Communications*, vol. 49, no. 17, pp. 1696–1698, 2013.

[78] R. W. Saalfrank, I. Bernt, E. Uller, and F. Hampel, "Template-mediated self assembly of six-and eight-membered iron coronates," *Angewandte Chemie International Edition*, vol. 36, no. 22, pp. 2482–2485, 1997.

[79] O. Waldmann, R. Koch, S. Schromm, J. Schülein, P. Müller, I. Bernt, R. W. Saalfrank, F. Hampel, and E. Balthes, "Magnetic anisotropy of a cyclic octanuclear Fe(III) cluster and magneto-structural correlations in molecular ferric wheels," *Inorganic chemistry*, vol. 40, no. 13, pp. 2986–2995, 2001.

[80] L. F. Jones, P. Jensen, B. Moubaraki, K. J. Berry, J. F. Boas, J. R. Pilbrow, and K. S. Murray, "Heptanuclear iron(III) triethanolamine clusters exhibiting millennium dome-like topologies and an octanuclear analogue with ground spin states of S= 5/2 and 0, respectively," *Journal of Materials Chemistry*, vol. 16, no. 26, pp. 2690–2697, 2006.

[81] M. Murugesu, K. A. Abboud, and G. Christou, "Preparation and properties of new Fe_6 and Fe_8 clusters of iron(III) with tripodal ligands," *Dalton Transactions*, no. 23, pp. 4552–4556, 2003.

[82] I. A. Gass, C. J. Milios, A. Collins, F. J. White, L. Budd, S. Parsons, M. Murrie, S. P. Perlepes, and E. K. Brechin, "Polymetallic clusters of iron(III) with derivatised salicylaldoximes," *Dalton Transactions*, no. 15, pp. 2043–2053, 2008.

[83] A. M. Ako, O. Waldmann, V. Mereacre, F. Klöwer, I. J. Hewitt, C. E. Anson, H. U. Güdel, and A. K. Powell, "Odd-numbered Fe^{III} complexes: synthesis, molecular structure, reactivity, and magnetic properties," *Inorganic chemistry*, vol. 46, no. 3, pp. 756–766, 2007.

[84] Bruker, "Saint," *Bruker AXS Inc., Madison, Wisconsin, USA*, 2007.

[85] A. M. M. Schreurs, "Peakref," *Utrecht University, The Netherlands*, 2005.

[86] A. L. Spek, "*PLATON* SQUEEZE: a tool for the calculation of the disordered solvent contribution to the calculated structure factors," *Acta Crystallographica Section C*, vol. 71, pp. 9–18, Jan 2015.

[87] L. Palatinus and G. Chapuis, "*SUPERFLIP* – a computer program for the solution of crystal structures by charge flipping in arbitrary dimensions," *Journal of Applied Crystallography*, vol. 40, pp. 786–790, Aug 2007.

[88] H. Lipson and M. M. Woolfson, "An extension of the use of intensity statistics," *Acta Crystallographica*, vol. 5, pp. 680–682, Sep 1952.

[89] D. Rogers and A. J. C. Wilson, "The probability distribution of X-ray intensities. V. A note on some hypersymmetric distributions," *Acta Crystallographica*, vol. 6, pp. 439–449, Jun 1953.

[90] M. C. Burla, R. Caliandro, B. Carrozzini, G. L. Cascarano, C. Cuocci, C. Giacovazzo, M. Mallamo, A. Mazzone, and G. Polidori, "Crystal structure determination and refinement *via SIR2014*," *Journal of Applied Crystallography*, vol. 48, pp. 306–309, Feb 2015.

[91] G. Cascarano, C. Giacovazzo, and M. Luić, "Direct methods and superstructures. I. Effects of the pseudotranslations on the reciprocal space," *Acta Crystallographica Section A*, vol. 41, pp. 544–551, Nov 1985.

[92] L. J. Barbour, "*LAYER* – a computer program for the graphic display of intensity data as simulated precession photographs," *Journal of Applied Crystallography*, vol. 32, pp. 351–352, Apr 1999.

[93] K. L. Taft, G. C. Papaefthymiou, and S. J. Lippard, "A mixed-valent polyiron oxo complex that models the biomineralization of the ferritin core," *Science*, vol. 259, no. 5099, pp. 1302–1305, 1993.

[94] N. Kojima, W. Aoki, M. Itoi, Y. Ono, M. Seto, Y. Kobayashi, and Y. Maeda, "Charge transfer phase transition and ferromagnetism in a mixed-valence iron complex, (n-C_3H_7)$_4$N[$Fe^{II}Fe^{III}$(dto)$_3$] (dto=$C_2O_2S_2$)," *Solid State Communications*, vol. 120, no. 4, pp. 165 – 170, 2001.

[95] R. Boča, I. Šalitroš, J. Kožíšek, J. Linares, J. Moncol', and F. Renz, "Spin crossover in a heptanuclear mixed-valence iron complex," *Dalton Transactions*, vol. 39, no. 9, pp. 2198–2200, 2010.

[96] A. Caneschi, A. Cornia, S. J. Lippard, G. C. Papaefthymiou, and R. Sessoli, "Magnetic properties of dodecanuclear mixed valence iron clusters," *Inorganica chimica acta*, vol. 243, no. 1-2, pp. 295–304, 1996.

[97] C. R. Groom, I. J. Bruno, M. P. Lightfoot, and S. C. Ward, "The Cambridge Structural Database," *Acta Crystallographica Section B: Structural Science, Crystal Engineering and Materials*, vol. 72, no. 2, pp. 171–179, 2016.

[98] J. A. van der Horn and M. Lutz, "Triethanolaminate iron perchlorate revisited: change of space group, chemical composition and oxidation states in [Fe_7(tea)$_3$(tea-H)$_3$](ClO_4)$_2$ (tea-H_3 is triethanolamine)," *Acta Crystallographica Section C*, vol. 74, Feb 2018. in press.

[99] S. Parsons, T. Wagner, O. Presly, P. A. Wood, and R. I. Cooper, "Applications of leverage analysis in structure refinement," *Journal of Applied Crystallography*, vol. 45, no. 3, pp. 417–429, 2012.

[100] P. W. Betteridge, J. R. Carruthers, R. I. Cooper, K. Prout, and D. J. Watkin, "*CRYSTALS* version 12: software for guided crystal structure analysis," *Journal of Applied Crystallography*, vol. 36, p. 1487, Dec 2003.

[101] H. D. Flack, "On enantiomorph-polarity estimation," *Acta Crystallographica Section A*, vol. 39, pp. 876–881, Nov 1983.

[102] R. E. Marsh, "Some thoughts on choosing the correct space group," *Acta Crystallographica Section B*, vol. 51, pp. 897–907, Dec 1995.

[103] F. L. Hirshfeld, "Can X-ray data distinguish bonding effects from vibrational smearing?," *Acta Crystallographica Section A*, vol. 32, pp. 239–244, Mar 1976.

[104] L. R. Falvello, "Jahn–Teller effects in solid-state co-ordination chemistry," *Journal of the Chemical Society, Dalton Transactions*, no. 23, pp. 4463–4476, 1997.

[105] S. Smeets, P. Parois, H.-B. Bürgi, and M. Lutz, "Temperature-dependent analysis of thermal motion, disorder and structures of tris(ethylenediamine)zinc(II) sulfate and tris(ethylenediamine)copper(II) sulfate," *Acta Crystallographica Section B*, vol. 67, pp. 53–62, Feb 2011.

[106] V. Schomaker and K. N. Trueblood, "Correlation of Internal Torsional Motion with Overall Molecular Motion in Crystals," *Acta Crystallographica Section B*, vol. 54, pp. 507–514, Oct 1998.

[107] G. M. Sheldrick, "A short history of SHELX," *Acta Crystallographica Section A: Foundations of Crystallography*, vol. 64, no. 1, pp. 112–122, 2008.

[108] W. Hummel, J. Hauser, and H.-B. Brgi, "PEANUT: Computer graphics program to represent atomic displacement parameters," *Journal of Molecular Graphics*, vol. 8, no. 4, pp. 214 – 220, 1990.

[109] L. M. J. Kroon-Batenburg, J. R. Helliwell, B. McMahon, and T. C. Terwilliger, "Raw diffraction data preservation and reuse: overview, update on practicalities and metadata requirements," *IUCrJ*, vol. 4, pp. 87–99, Jan 2017.